Fast high-order algorithms and well-conditioned integral equations for high-frequency sound-hard scattering problems

Oscar Bruno, Tim Elling, Catalin Turc
bruno@caltech.edu, elling@caltech.edu, catalin.turc@case.edu

Abstract

This text introduces 1) New Regularized Combined Field Integral Equations (CFIE-R) for the solution of frequency-domain sound-hard scattering problems, and, 2) Fast, high-order algorithms for the numerical solution of the CFIE-R and related integral equations. Like the classical Combined Field Integral Equation (CFIE), the CFIE-R are unikely-solvable integral equations based on use of single and double layer potentials. Unlike the CFIE, however, the CFIE-R utilize a composition of the double-layer potential with a regularizing operator that gives rise to highly-favorable spectral properties—thus making it possible to produce accurate solutions by means of iterative solvers in *small numbers of iterations*. The CFIE-R-based fast high-order integral algorithms introduced in this text enable highly accurate solution of challenging sound-hard scattering problems, including hundred-wavelength cases, in single-processor runs on present-day desktop computers. A variety of numerical results demonstrate the qualities of the numerical solvers as well as the advantages that arise from the new integral equation formulation.

Keywords: acoustic scattering, Combined Field Integral Equations, pseudodifferential operators.

1 Introduction

The boundary-integral methods of computational acoustics possess excellent qualities. Most notably, boundary integral equations require much smaller discretizations, for a given accuracy, than the three-dimensional discretizations implicit in finite-element or finite-difference approximations of the associated partial differential equations, and they automatically enforce the condition of radiation at infinity. While integral equations do not give rise to sparse systems of linear equations, the smaller-sized associated boundary discretizations can be exploited through use of fast iterative solvers [6, 9, 29, 31] based on Krylov-subspace linear algebra solvers [30], leading to algorithms that can outperform their volumetric PDE-approximating counterparts to very significant extents.

In the present contribution we consider the problem of scattering by obstacles in the challenging sound-hard case in three dimensions. We introduce a fast high-order integral algorithm for this problem whose performance is similar to that arising from the sound-soft method [9]: super-algebraic convergence and $N^\alpha \log N$ cost (with $6/5 \leq \alpha \leq 4/3$, where N is the size of the surface discretization). In particular, we address the exacting characteristics of the sound hard problem through introduction of a new uniquely-solvable Regularized Combined Field Integral Equations (CFIE-R), and we generalize the accelerator and the high-order accurate integrators introduced in [9] to enable applicability to the significantly more singular integrals that compose both the CFIE-R and the classical Combined Field Integral Equation (CFIE). In view of the reduced numbers of iterations required for iterative solution of the CFIE-R equations and the accurate and efficient evaluation

of integral operators provided by our integration algorithms, the fast high-order solvers introduced in this text enable, for the first time, highly accurate solution of hundred-wavelength sound-hard scattering problems in present-day single processors.

The CFIE-R integral equations we introduce are also applicable to two-dimensional problems. To illustrate this point we present, in addition to the algorithms mentioned above for three dimensional problems, CFIR-R algorithms applicable to Neumann problems in the plane. The numerical implementation we use in this case is based on the Nyström methodology introduced in [23]: global trigonometric approximations of the densities and closed-form integration of products of single Fourier harmonics and the most singular part of the integral kernels. The two-dimensional hypersingular operator is expressed as a Cauchy Principal Value operator and analytic integration is again used to obtain the integrals of products of singular kernels (related to the kernels of the one-dimensional Hilbert transform) and Fourier harmonics.

A class of combined-field equations has been proposed for treatment of problems of scattering by sound-soft and sound-hard obstacles. Unlike other formulations, the Combined Field Integral Equations (which result from representations of acoustic fields by means of *combined* single- and double-layer potentials [13, 22]) possess the critical property of unique solvability. For the Neumann boundary conditions related with the sound-hard case considered in this paper, normal derivatives of double layer potentials, and associated hypersingular kernels and operators, are part of the CFIE formulations. As it is known, the eigenvalues of such operators accumulate at infinity. As a result, iterative solvers based on such integral formulations require numbers of iterations that grow significantly as discretization sizes and/or frequencies are increased.

A number of strategies have been proposed to address these difficulties, including algebraic preconditioners and formulations based on use of pseudoinverses. The generic algebraic preconditioning strategies (such as multi-grid methods [17] or Frobenius norm minimizations and sparsification techniques [5, 18, 34]) which are not specifically geared towards solution of wave scattering problems, typically encounter convergence breakdowns at higher-frequencies and large-discretizations [25, 33]. Methods based on use of pseudoinverses that invert the hypersingular operator modulo compact operators have been found effective [2, 3] in reducing the numbers of Krylov-subspace iterations. Unfortunately, the evaluation of the pseudoinverses, which is based on explicit inversion of a discrete Laplace operator on the scattering boundary by means of a boundary-element formulation, can be expensive, and it does not lend itself easily for use in conjuncion with fast, high-order methods [9] that we use and develop in the present contribution.

Our approach is based on representation of the scattered field as a sum of the single layer potential, and composition of the double layer potential with a regularizing operator. Use of such a representation for the Neumann problem gives rise to certain Regularized Combined Field Integral Equations (CFIE-R) that are reminiscent of the classical CFIE—except for the fact that the acoustic hypersingular operator acts on the regularizing operator. Our choice of the regularizing is motivated by our goal to a) Stabilize the leading order effect of the hypersingular operator—so that the integral operators arising in CFIE-R are Fredholm and their spectra are bounded away from infinity, while b) Obtaining for the CFIE-R the unique solvability characteristic of the classical CFIE. As shown in this text, both of these properties can be guaranteed through selection of rather simple regularizing operators: Use of *single layer potentials* S_K of any wavenumber K, equal or different from the wavenumber $k = 2\pi/\lambda$ inherent in the given scattering problem, satisfactorily addresses point a); selection of *imaginary wavenumbers* K in the definition of regularizing operators S_K, on the other hand, makes the CFIE-R formulations uniquely solvable. In practice the CFIE-R coupling parameters and imaginary wavenumbers K can and should be selected in such a way that

the spectral distribution of the resulting equations enables optimally small number of linear algebra iterations.

(A regularizing operator equal to the *zero-frequency* single layer operator S_0 was used in [1, 14, 28] to bypass evaluation of hypersingular operators and to obtain well-conditioned integral equations. As shown in Table 6 below, use of the regularizer proposed in this text, S_K with $K = ik = 2\pi i/\lambda$, gives rise to significantly faster iterative solution than use of the regularizer S_0, with gains in computing times that increase with frequency. In particular, use of the S_K regularizer in our context yields improvements by factors of 1.6, 2.6 and 3.7 in the numbers of iterations and factors of 1.2, 2.5 and 3.4 in computing times over those resulting for the regularizer S_0, for a similar accuracy, for scatterers of acoustical sizes of 10.2λ, 50λ and 100λ, respectively.)

We demonstrate the properties of the new integral formulations and numerical implementations for a variety of convex and non-convex scattering two- and three-dimensional bodies in the mid to high-frequency regime. In particular these results show that the regularized equations we propose possess excellent spectral distributions, as attested by the fact that the number of iterations required by a GMRES solver to reach a certain residual varies very mildly with the type of scattering surface and the acoustical size of the problems. In particular, the number of iterations required by the CFIE-R equations compares very favorably with those required by the classical CFIE and other previous formulations. To place these findings in a true perspective we additionally note that one matrix-vector product in our CFIE-R three-dimensional implementations is only 1.6 times more costly, in terms of computing times, than one matrix-vector product in the implementation of the CFIE for the same discretization (and with essentially identical accuracies). These significant gains in computational costs together with the excellent accuracy enabled by the fast high-order introduced in this work make the CFIE-R formulations extremely attractive alternatives to classical CFIE for sound-hard scattering problems from smooth and closed surfaces in the mid to high-frequency regime.

This paper is organized as follows: in Section 2 we introduce our novel Regularized Combined Field Integral Equations, in Section 3 we discussed criteria to obtain coupling parameters that lead to operators with excellent spectral clustering properties, in Sections 4 we present the numerical algorithm, while numerical results are presented in Section 5.

2 Sound-Hard Regularized Combined Field Integral Equations

2.1. Sound-Hard Scattering Problem. We consider the problem of scattering of acoustic waves by a bounded obstacle Ω in d dimensional space ($d = 2, 3$). The corresponding scattered field u^s satisfies the Helmholtz equation in the exterior of Ω together with Neumann boundary conditions on the boundary Γ of Ω and a condition of radiation at infinity,

$$\Delta u^s + k^2 u^s = 0 \text{ in } \mathbb{R}^d \setminus \Omega \tag{1}$$

$$\frac{\partial u^s}{\partial n} = -\frac{\partial u^{inc}}{\partial n} \text{ on } \Gamma \tag{2}$$

$$\lim_{|r|\to\infty} r^{(d-1)/2}(\partial u^s/\partial r - iku^s) = 0, \text{ for } d = 2, 3, \tag{3}$$

where u^{inc} denotes the incident acoustic field. For simplicity in this text we assume the boundary Γ is smooth.

2.2. Integral Operators and Classical Integral Equations. A classical Indirect Combined Field Integral Equation formulation (ICFIE), which was originally introduced by Brakhage and

Werner [7] and Panich [28], assumes a representation of the scattered field as a combination of single and double layer potentials of the form

$$u^s(\mathbf{z}) = -i\eta \int_\Gamma G_k(\mathbf{z}-\mathbf{y})\phi(\mathbf{y})ds(\mathbf{y}) + \int_\Gamma \frac{\partial G_k(\mathbf{z}-\mathbf{y})}{\partial \mathbf{n}(\mathbf{y})}\phi(\mathbf{y})ds(\mathbf{y}) \tag{4}$$

for a density ϕ, where $\eta \neq 0$ is a coupling parameter and where G_k denotes the outgoing free-space Green's function for $d = 2, 3$,

$$G_k(\mathbf{z}-\mathbf{y}) = \frac{i}{4}H_0^1(k|\mathbf{z}-\mathbf{y}|) \quad (d=2) \quad ; \quad G_k(\mathbf{z}-\mathbf{y}) = \frac{e^{ik|\mathbf{z}-\mathbf{y}|}}{4\pi|\mathbf{z}-\mathbf{y}|} \quad (d=3). \tag{5}$$

Taking the normal derivative of both sides of (4) and using the sound-hard boundary condition, in view of well known expressions for the boundary values of the normal derivative of the layer potentials there results the ICFIE

$$i\eta\frac{\phi(\mathbf{x})}{2} - i\eta(D_k'\phi)(\mathbf{x}) + (N_k\phi)(\mathbf{x}) = -\frac{\partial u^{\rm inc}(\mathbf{x})}{\partial \mathbf{n}(\mathbf{x})} \ , \ \mathbf{x} \in \Gamma \tag{6}$$

(which called the "Indirect" differentiate it from the corresponding "Direct" CFIE, which is given by equation (22) with $\mathcal{R}$ equal to the identity operator I). Here D_k' and N_k denote the *normal derivative of the single layer* and the *normal derivative of the double layer* (or *hypersingular*) operators on Γ: for $x \in \Gamma$ and letting the acronym "PV" denote Cauchy Principal Value integrals, we have

$$(D_k'\phi)(\mathbf{x}) = \int_\Gamma \frac{\partial G_k(\mathbf{x}-\mathbf{y})}{\partial \mathbf{n}(\mathbf{x})}\phi(\mathbf{y})ds(\mathbf{y}) \qquad \text{and} \qquad (N_k\phi)(\mathbf{x}) = {\rm PV}\int_\Gamma \frac{\partial^2 G_k(\mathbf{x}-\mathbf{y})}{\partial \mathbf{n}(\mathbf{x})\partial \mathbf{n}(\mathbf{y})}\phi(\mathbf{y})ds(\mathbf{y}). \tag{7}$$

The hypersingular operator N_k can be expressed in terms of operators that require differentiation in the tangential direction only [22]: for $d = 2$ we have

$$(N_k\phi)(\mathbf{x}) = k^2\int_\Gamma G_k(\mathbf{x}-\mathbf{y})(\mathbf{n}(\mathbf{x})\cdot\mathbf{n}(\mathbf{y}))\phi(\mathbf{y})ds(\mathbf{y}) + {\rm PV}\int_\Gamma \partial_{s_\mathbf{x}}G_k(\mathbf{x}-\mathbf{y})\partial_{s_\mathbf{y}}\phi(\mathbf{y})ds(\mathbf{y}) \tag{8}$$

where $\partial_{s_\mathbf{x}}$ and $\partial_{s_\mathbf{y}}$ denote the operators of tangential $\mathbf{x}$ and $\mathbf{y}$ differentiation on Γ, respectively; the corresponding expression for $d = 3$ is given by

$$(N_k\phi)(\mathbf{x}) = k^2\int_\Gamma G_k(\mathbf{x}-\mathbf{y})(\mathbf{n}(\mathbf{x})\cdot\mathbf{n}(\mathbf{y}))\phi(\mathbf{y})d\sigma(\mathbf{y}) + {\rm PV}\int_\Gamma \overrightarrow{\rm curl}_\Gamma^{\mathbf{x}}\, G_k(\mathbf{x}-\mathbf{y})\cdot\overrightarrow{\rm curl}_\Gamma^{\mathbf{y}}\,\phi(\mathbf{y})d\sigma(\mathbf{y}) \tag{9}$$

where, letting $\nabla_\Gamma^\mathbf{z}$ denote the tangential gradient on Γ with respect to a variable $\mathbf{z}$ ($\mathbf{z} = \mathbf{x}$ or $\mathbf{z} = \mathbf{y}$), the tangential rotational operator $\overrightarrow{\rm curl}_\Gamma^\mathbf{z}$ with respect to the variable $\mathbf{z}$ is given by $\overrightarrow{\rm curl}_\Gamma^\mathbf{z}\phi = (\nabla_\Gamma^\mathbf{z}\phi)\times\mathbf{n}(\mathbf{z})$ [27]. As is well known, the ICFIE is a uniquely solvable integral equation for all real values of the wavenumber k [22, 27].

In addition to the single-layer-normal-derivative and hypersingular operators D_k' and N_k, our regularized combined field equations rely on use of the single layer operator S_K *with wavenumber* K, which, for a density function ψ defined on Γ is given by

$$(S_K\psi)(\mathbf{x}) = \int_\Gamma G_K(\mathbf{x}-\mathbf{y})\psi(\mathbf{y})ds(\mathbf{y}) \ , \ \mathbf{x} \in \Gamma. \tag{10}$$

Note that, for purposes of regularization, the wavenumber K in equation (10) may be any real or complex number and, in particular, it may differ from the physical wavenumber k. For $d = 2$ we will also use the $k = 0$ modified single layer operator

$$(S_0^C\psi)(\mathbf{x}) = -\frac{1}{2\pi}\int_\Gamma \log(|\mathbf{x}-\mathbf{y}|/C)\psi(\mathbf{y})ds(\mathbf{y})\ ,\ \mathbf{x}\in\Gamma, \tag{11}$$

where C is an arbitrary positive number.

2.3. Regularized Combined Field Integral Equations ICFIE-R and DCFIE-R. As mentioned in the previous section, the ICFIE is a uniquely solvable integral equation for all real values of the wavenumber k. Yet, as it contains the operator N_k, the overall operator on the left hand side of equation (6) has pseudo-differential order one [27]—and, therefore, its eigenvalues accumulate at infinity. As a result, the numerical solution of discrete versions of the ICFIE by means of iterative linear algebra solvers often requires exceedingly large numbers of iterations even for modest acoustical sizes (see e.g. Tables 1 and 5 below), and, further, it gives rise to iteration numbers that increase significantly with frequency.

To produce integral equations with mild spectral character we use representations of the scattered fields in which the double layer potential is composed with an appropriate regularizing operator—so that the ill effects arising from the hypersingular operator N_k and its first-order pseudo-differential character are eliminated. In detail, using a regularizing operator $\mathcal{R}$ we represent the scattered field by means of the expression

$$u^s(\mathbf{z}) = \int_\Gamma \left(-i\eta G_k(\mathbf{z}-\mathbf{y})\mu(\mathbf{y}) + \frac{\partial G_k(\mathbf{z}-\mathbf{y})}{\partial \mathbf{n}(\mathbf{y})}(\mathcal{R}\mu)(\mathbf{y})\right) ds(\mathbf{y}), \tag{12}$$

which leads to the Regularized Combined Field Integral Equation formulation (ICFIE-R):

$$i\eta\frac{\mu(\mathbf{x})}{2} - i\eta(D_k'\mu)(\mathbf{x}) + (N_k\circ\mathcal{R})\mu(\mathbf{x}) = -\frac{\partial u^{\rm inc}(\mathbf{x})}{\partial \mathbf{n}(\mathbf{x})}\ ,\ \mathbf{x}\in\Gamma. \tag{13}$$

If the operator $\mathcal{R}$ is chosen to be a pseudoinverse of the operator N_k, i.e. $N_k\circ\mathcal{R} = I + \text{Compact}$ in the natural space $H^{m-\frac{1}{2}}(\Gamma)$ $(m \geq 0)$ of boundary values for the Helmholtz equation, then the operator on the left hand side of equation (13) is itself a compact perturbation of a multiple of identity—and, therefore, on account of the Fredholm theory, the ICFIE-R left-hand-side operator is invertible if and only if it is injective. And, importantly, upon appropriate choices of regularizing operator $\mathcal{R}$, significant reductions in iteration numbers can thereby be achieved.

In these regards we have the following theorem.

Theorem 2.1 *Let $k \geq 0$ and let $\mathcal{R}$ be one of the following operators: $\mathcal{R} = S_K$ with $K = ik_1$, for any $k_1 > 0$ for $d = 2$ or any $k_1 \geq 0$ for $d = 3$, or $\mathcal{R} = S_0^C$ for the case $d = 2$, where C is any number larger than the capacity of Γ (it suffices to take C larger than the diameter of Γ, which is not smaller than its capacity). Then, the left-hand-side operator*

$$\frac{i\eta}{2}I - i\eta D_k' + N_k\circ\mathcal{R} \tag{14}$$

equals the sum of a multiple of the identity and a compact operator, and it is invertible in $H^{m-\frac{1}{2}}(\Gamma)$, with a continuous inverse for all $m \geq 0$.

Proof. Let N_K, S_K and D'_K be the hypersingular, single-layer, and single-layer-normal-derivative operators with wavenumber K. Our proof is based on use of the Calderón identity [16]

$$N_K \circ S_K = -\frac{I}{4} + (D'_K)^2 \tag{15}$$

which is valid for all values of K. In the case $d = 2$, further, since, in view of equation (8) the constant functions are in the kernel of the operator N_0, from (15) we also obtain the $K = 0$ relation

$$N_0 \circ S_0^C = -\frac{I}{4} + (D'_0)^2. \tag{16}$$

Using equations (15) for $K = ik_1$ with any $k_1 > 0$ for $d = 2$ or any $k_1 \geq 0$ for $d = 3$ we obtain

$$N_k \circ S_K = (N_k - N_K) \circ S_K + N_K \circ S_K = -\frac{I}{4} + (N_k - N_K) \circ S_K + (D'_K)^2 = -\frac{I}{4} + \mathcal{A}. \tag{17}$$

Analogously, from equation (16) for $d = 2$ we obtain

$$N_k \circ S_0^C = (N_k - N_0) \circ S_0^C + N_0 \circ S_0^C = -\frac{I}{4} + (N_k - N_0) \circ S_0^C + (D'_0)^2 = -\frac{I}{4} + \mathcal{B} \tag{18}$$

Each one of the operators $\mathcal{A}$ and $\mathcal{B}$ in (17) and (18) equals the sum of two compact operators. Indeed, for $K = ik_1$ with $k_1 \geq 0$ the operator D'_K maps $H^{m-\frac{1}{2}}(\Gamma)$ into $H^{m+\frac{1}{2}}(\Gamma)$, and, thus, $(D'_K)^2 : H^{m-\frac{1}{2}}(\Gamma) \to H^{m+\frac{3}{2}}(\Gamma) \hookrightarrow H^{m-\frac{1}{2}}(\Gamma)$ is a compact operator [27]; similarly the integral kernel of the operator $N_k - N_K$ is weakly singular and thus the composition $(N_k - N_K) \circ S_K : H^{m-\frac{1}{2}}(\Gamma) \to H^{m+\frac{1}{2}}(\Gamma) \hookrightarrow H^{m-\frac{1}{2}}(\Gamma)$ is also compact. The left-hand-side operator (14) thus equals the sum of a multiple of the identity operator plus a compact operator—since D'_k is itself a compact operator. In view of the Fredholm alternative, then, in order to show this operator is invertible it suffices to establish its injectivity.

To do this let μ be a solution to the homogeneous equation (13), and let us call u^+ (resp. u^-) the potential defined for $\mathbf{z}$ outside Ω (resp. $\mathbf{z} \in \Omega$) by the right hand side of equation (12). Clearly, u^+ is a radiative solution to the Helmholtz problem in the exterior of Ω with $\partial u^+/\partial \mathbf{n} = 0$ on Γ. We conclude that $u^+ = 0$ everywhere outside Ω. From the classical jump relations for the boundary values of layer potentials we see that

$$-u^- = \mathcal{R}\mu = S_K \mu \quad , \quad -\frac{\partial u^-}{\partial \mathbf{n}} = -i\eta\ \mu \quad \text{on } \Gamma\ .$$

Using Green's identities we then obtain

$$i\eta \int_\Gamma (S_K \mu)\bar{\mu} ds = \int_\Gamma u^- \overline{\frac{\partial u^-}{\partial \mathbf{n}}} ds = \int_\Omega (|\nabla u^-|^2 - k^2 |u^-|^2) dx, \tag{19}$$

and, thus,

$$\int_\Gamma (S_K \mu)\bar{\mu} ds = 0. \tag{20}$$

To conclude the proof we must show that $\mu = 0$. We do this first in the cases $k_1 > 0$ for $d = 2$ and $k_1 \geq 0$ for $d = 3$, for which we know that the single layer operator $\mathcal{R} = S_K$ is coercive (see e.g. [26, 27, p. 269]), i.e.

$$\int_\Gamma (S_{ik_1} \mu)\bar{\mu} ds \geq ||\mu||_{H^{-\frac{1}{2}}(\Gamma)}. \tag{21}$$

Clearly, from equations (20) and (21) we have $\mu = 0$ and our result follows in these cases. The case $k_1 = 0$ for $d = 2$ can be treated similarly, using, this time, that the operator S_0^C is positive and bounded below [26, p. 264]. The proof is now complete. ∎

Remark 2.2 *It follows from Theorem 2.1 that the spectrum of left-hand-side operator* (14) *is bounded away from zero and infinity. This, fact, which is illustrated in Figure 1, has a significant impact on the numbers of iterations required by iterative solvers for equation* (13)*; see e.g. Tables 1 and 5.*

Remark 2.3 *Although this paper focuses mainly on regularization of the "Indirect" integral equations* (6)*, leading to the regularized equation* (13)*, a similar treatment can be applied to the corresponding Direct Combined Field Integral Equation (DCFIE) for the unknown boundary values on* Γ *of the total field* u*. Like the classical and regularized indirect equations, the corresponding direct equations (which are called DCFIE and DCFIE-R in this paper) are uniquely solvable—as it can be shown by means of duality arguments (cf. [22, p. 104] for a proof in the classical DCFIE case and [10] for the corresponding treatment of classical and regularized equations in the analogous electromagnetic context). The classical DCFIE and regularized DCFIE-R equations can be expressed in the form*

$$\frac{i\eta}{2}u(\mathbf{x}) - i\eta(D_k\ u)(\mathbf{x}) - (\mathcal{R}\circ N_k)u(\mathbf{x}) = i\eta\, u^{\rm inc}(\mathbf{x}) + \mathcal{R}(\frac{\partial u^{\rm inc}(\mathbf{x})}{\partial \mathbf{n}(\mathbf{x})}) \tag{22}$$

with $\mathcal{R} = I$ *and* $\mathcal{R} = S_K$*, respectively, where the operator* D_k*, which equals the transpose of* D_k'*, denotes the classical double layer potential. (See Section 2.4 with regards to the selection of the parameter* K*.) As illustrated briefly in Table 4 and as we verified in a wide range of cases at both, high and low frequencies, the properties (accuracy and cost) of the ICFIE-R and DCFIE-R equations are virtually identical.*

2.4. ICFIE-R and DCFIE-R parameter selection. We have observed in practice that use of the parameters

$$k_1 = k \text{ in } 2D,\ k_1 = k/2 \text{ in } 3D,\ \eta = 1 \tag{23}$$

in equation (13) leads, upon discretization, to finite-dimensional linear systems which can be solved in very small number of iterations by means of the iterative solver GMRES.

Having discussed our main regularization technique, we now turn to the high-order Nyström methods we use to discretize the integral operators that appear in equations (6) and (13). In the two-dimensional case, which is discussed in the following section, our discretization approach amounts to a rather direct extension of the methodology introduced in [23]. To treat the three-dimensional case, in turn, we introduce, in Section 5, a suitable generalization of the approach [8].

3 ICFIE and ICFIE-R operators re-expressed: weakly-singular kernels and differential operators

In order to evaluate numerically the the left hand side of equation (13) for a given density μ in the three-dimensional case we re-express the hypersingular operators N_k defined by equations (9) in a form that only involves weakly singular kernels and differential operators. Specifically, using

integration by parts in equation (9) we obtain [27, p. 143]

$$\begin{aligned}(N_k\mu)(\mathbf{x}) &= \int_\Gamma G_k(\mathbf{x}-\mathbf{y})\Delta_\Gamma\mu(\mathbf{y})d\sigma(\mathbf{y}) \\ &+ \int_\Gamma \nabla_\Gamma\mu(\mathbf{y})\cdot\nabla^{\mathbf{y}}G_k(\mathbf{x}-\mathbf{y})(1-\mathbf{n}(\mathbf{x})\cdot\mathbf{n}(\mathbf{y}))d\sigma(\mathbf{y}) \\ &+ \int_\Gamma \frac{\partial G_k(\mathbf{x}-\mathbf{y})}{\partial\mathbf{n}(\mathbf{y})}\nabla_\Gamma\mu(\mathbf{y})\cdot\mathbf{n}(\mathbf{x})d\sigma(\mathbf{y}) \\ &+ k^2\int_\Gamma G_k(\mathbf{x}-\mathbf{y})\mu(\mathbf{y})(\mathbf{n}(\mathbf{x})\cdot\mathbf{n}(\mathbf{y}))d\sigma(\mathbf{y}) \end{aligned} \tag{24}$$

where $\Delta_\Gamma = \mathrm{div}_\Gamma\nabla_\Gamma$ denotes the surface Laplace-Beltrami operator on Γ. For smooth surfaces we clearly have $|1-\mathbf{n}(\mathbf{x})\cdot\mathbf{n}(\mathbf{y})| = \mathcal{O}(|\mathbf{x}-\mathbf{y}|)$, and therefore all the kernels involved in the integrals operators are weakly singular and, importantly, of order $\mathcal{O}(|\mathbf{x}-\mathbf{y}|^{-1})$. Using equation (24) we may thus evaluate the composition of operators on the left-hand side of equation (13) (with $\mathcal{R} = S_{ik_1}$) as a sequence of operations, each one of which amounts to evaluation of either an integral operator with a singular kernel or a surface differentiation operator; the action of these operators can in turn be obtained numerically, with high-order accuracy, through use of partitions of unity and a local polar-integration algorithm for resolution of integrable singularities [8], together with Fourier expansions of smoothly localized densities for differentiation [10], as discussed in Section 5.

An alternative algorithm can be used for the evaluation of the composition of operators in (13) (with $\mathcal{R} = S_{ik_1}$) that does not require use of numerical differentiation. Indeed, in view of the Calderón identity (15) we have

$$N_k\mathcal{R} = N_k\ S_{ik_1} = (N_k - N_{ik_1})S_{ik_1} + N_{ik_1}S_{ik_1} = (N_k - N_{ik_1})S_{ik_1} - \frac{I}{4} + (D'_{ik_1})^2. \tag{25}$$

Clearly, the operator

$$N_k - N_{ik_1} = (N_k - N_0) - (N_{ik_1} - N_0) \tag{26}$$

can be expressed in terms of the $\mathcal{O}(|\mathbf{x}-\mathbf{y}|^{-1})$ kernels

$$\frac{\partial^2(G_k(\mathbf{x}-\mathbf{y}) - G_0(\mathbf{x}-\mathbf{y}))}{\partial\mathbf{n}(\mathbf{x})\partial\mathbf{n}(\mathbf{y})} \quad \text{and} \quad \frac{\partial^2(G_{ik_1}(\mathbf{x}-\mathbf{y}) - G_0(\mathbf{x}-\mathbf{y}))}{\partial\mathbf{n}(\mathbf{x})\partial\mathbf{n}(\mathbf{y})}$$

and, thus, the complete right-hand side in equation (25) can be produced numerically by means of the high-order integration algorithm [8] without recourse to evaluation of surface derivatives of the unknown density μ.

The relative advantages of the two approaches described above for evaluation of the composition of operators in (13) are discussed in Remark 5.5. One particular advantage of the second approach is discussed in [12] in the case of scattering problems in domains with corners.

4 High-order Nyström discretization I: Two-dimensional problems

The Nyström approach [23] was developed to treat equation (6) in the two-dimensional case. In order to extend this methodology to the two-dimensional regularized equation (13), in turn, it is necessary to provide a method for evaluation of the single-layer potential corresponding to an

imaginary wavenumber $K = ik_1$. We do this in what follows and, for the sake of completeness, we briefly lay down the main elements of the methodology [23].

According to [23], using a smooth 2π-periodic parametrization $x = x(t)$ of the boundary curve Γ, equation (6) can be expressed in the form

$$\frac{1}{4\pi}\int_0^{2\pi} \cot\frac{\tau-t}{2}\psi'(\tau)d\tau + \int_0^{2\pi} L(t,\tau)\psi(\tau)d\tau + i\eta|x'(t)|\frac{\psi(t)}{2} = |x'(t)|g(x(t)) \tag{27}$$

where $\psi(t) \equiv \mu(x(t))$, $g = -\frac{\partial u^{\rm inc}}{\partial \mathbf{n}}$, and where the kernel $L(t,\tau)$ is given by

$$L(t,\tau) = k^2 M_k(t,\tau)x'(t)\cdot x'(\tau) - N(t,\tau) - i\eta H(t,\tau) = P(t,\tau) - i\eta H(t,\tau) \tag{28}$$

with

$$\begin{aligned} M_K(t,\tau) &= \frac{i}{4}H_0^{(1)}(K|x(t)-x(\tau)|) \\ H(t,\tau) &= \frac{ik}{4}\mathbf{n}(t)\cdot(x(t)-x(\tau))\frac{H_1^{(1)}(k|x(t)-x(\tau)|)}{|x(t)-x(\tau)|}|x'(\tau)||x'(t)| \\ N(t,\tau) &= \frac{\partial^2}{\partial t\,\partial\tau}\left\{\frac{i}{4}H_0^{(1)}(k|x(t)-x(\tau)|) + \frac{1}{4\pi}\ln\left(4\sin^2\frac{t-\tau}{2}\right)\right\}, \end{aligned} \tag{29}$$

and $K = k$ (cf. equation (32)). The kernel L can be expressed in the form

$$L(t,\tau) = L_1(t,\tau)\ln\left(4\sin^2\frac{t-\tau}{2}\right) + L_2(t,\tau) \tag{30}$$

where the functions L_1 and L_2 are smooth, and, even, analytic, if the curve Γ itself is analytic [23]. Using trigonometric interpolation for the periodic density ψ in (27) and explit formulas for integration of products of each one the singular kernels $\ln\left(4\sin^2\frac{t-\tau}{2}\right)$ and $\cot\frac{\tau-t}{2}$ and Fourier harmonics $e^{im\tau}$, the discretization of equation (27) leads to the linear system

$$\begin{aligned} \sum_{j=0}^{2n-1} & \psi(t_j^{(n)})\left\{T^{(n)}_{\ell-j} + R^{(n)}_{|\ell-j|}L_1(t_\ell^{(n)},t_j^{(n)}) + \frac{\pi}{n}L_2(t_\ell^{(n)},t_j^{(n)})\right\} \\ + \;& i\eta|x'(t_\ell^{(n)})|\psi(t_\ell^{(n)}) = |x'(t_\ell^{(n)})|g(x(t_\ell^{(n)})),\ \ell = 0,1,\ldots,2n-1, \end{aligned} \tag{31}$$

where $t_j^{(n)} = \frac{j\pi}{n}$ are equispaced discretization points, and where the weights $T^{(n)}$ and $R^{(n)}$ are given by

$$T_j^{(n)} = \begin{cases} \frac{1}{2n\sin^2(t_j^{(n)}/2)}, & j \text{ odd} \\ 0, & j \text{ even}, j \neq 0 \\ -\frac{n}{2}, & j = 0, \end{cases}$$

and

$$R_j^{(n)} = -\frac{2\pi}{n}\sum_{m=1}^{n-1}\frac{1}{m}\cos\frac{mj\pi}{n} - \frac{(-1)^j\pi}{n^2}.$$

A quadrature rule similar to the one outlined above in this section for the operator in equation (6) could be put forth for integration of the kernel M_K for imaginary values $K = ik_1$: the kernel of the operator

$$(S_{ik_1}\phi)(x(t)) = \int_0^{2\pi} M_{ik_1}(t,\tau)|x'(\tau)|\phi(x(\tau))d\tau, \tag{32}$$

can be expressed in a form similar to equation (30):

$$M_{ik_1}(t,\tau) = \tilde{M}_1(t,\tau)\ln\left(4\sin^2\frac{t-\tau}{2}\right) + \tilde{M}_2(t,\tau), \tag{33}$$

where $\tilde{M}_1(t,\tau) = -\frac{1}{4\pi}J_0(ik_1|x(t)-x(\tau)|)$, and where $\tilde{M}_2$ is a smooth function defined by equation (33). Unfortunately, however, the modified Bessel function $I_0(x) = J_0(ix)$, and thus the kernels $\tilde{M}_1$ and $\tilde{M}_2$, grow exponentially with their arguments, while M_{ik_1} actually decays exponentially, and thus the splitting strategy inherent in equation (33) generally gives rise to significant cancellation errors, if used throughout the integration domain.

In order to avoid subtraction of exponentially large quantities, we evaluate the operator M_{ik_1} by means of a slight modification of the approach used for the operator L: instead of (33) we use the truncated decomposition

$$\begin{aligned} M_{ik_1}(t,\tau) &= e^{-k_1|x(t)-x(\tau)|^4}\left\{\tilde{M}_1(t,\tau)\ln\left(4\sin^2\frac{t-\tau}{2}\right) + \tilde{M}_2(t,\tau)\right\} \\ &+ (1-e^{-k_1|x(t)-x(\tau)|^4})M_{ik_1}(t,\tau) \end{aligned} \tag{34}$$

which, as can be checked easily, does not suffer from cancellation errors. Using (34) we obtain a high-order quadrature rule for the operator S_{ik_1}:

$$\begin{aligned} (S_{ik_1}\phi)(x(t_\ell^{(n)})) &\approx \sum_{j=0}^{2n-1}\psi(t_j^{(n)})|x'(t_j^{(n)})|\left\{R^{(n)}_{|\ell-j|}\tilde{M}_1(t_\ell^{(n)},t_j^{(n)})\chi(t_\ell^{(n)},t_j^{(n)})\right. \\ &+ \left.\frac{\pi}{n}\left(\tilde{M}_2(t_\ell^{(n)},t_j^{(n)})\chi(t_\ell^{(n)},t_j^{(n)}) + \tilde{M}(t_\ell^{(n)},t_j^{(n)})[1-\chi(t_\ell^{(n)},t_j^{(n)}]\right)\right\} \\ &= \sum_{j=0}^{2n-1}\psi(t_j^{(n)})|x'(t_j^{(n)})|\ SI^{(n)}(t_\ell^{(n)},t_j^{(n)},|\ell-j|) \end{aligned} \tag{35}$$

where $\chi(t_\ell^{(n)},t_j^{(n)}) = e^{-k_1|x(t_\ell^{(n)})-x(t_j^{(n)})|^4}$. Based on equation (31) and (35) we obtain the following discretization of (13) with $\mathcal{R} = S_{ik_1}$:

$$\begin{aligned} &\sum_{j=0}^{2n-1} -i\eta\psi(t_j^{(n)})\left\{R^{(n)}_{|\ell-j|}H_1(t_\ell^{(n)},t_j^{(n)}) + \frac{\pi}{n}H_2(t_\ell^{(n)},t_j^{(n)})\right\} \\ &+\sum_{j=0}^{2n-1}\left(\sum_{m=0}^{2n-1}\psi(t_m^{(n)})|x'(t_m^{(n)})|\ SI^{(n)}(t_j^{(n)},t_m^{(n)},|j-m|)\right)\times \\ &\left\{T^{(n)}_{\ell-j} + R^{(n)}_{|\ell-j|}P_1(t_\ell^{(n)},t_j^{(n)}) + \frac{\pi}{n}P_2(t_\ell^{(n)},t_j^{(n)})\right\} \\ &+ i\eta|x'(t_\ell^{(n)})|\psi(t_\ell^{(n)}) = |x'(t_\ell^{(n)})|g(x(t_\ell^{(n)})),\ \ell = 0,1,\ldots,2n-1. \end{aligned} \tag{36, 37}$$

5 Fast, high-order Nyström discretization II: Three-dimensional problems

As shown in what follows, in the three dimensional case, the integral operators that enter the Combined Field Equations (6) and (13) can be evaluated efficiently, with high-order accuracy and

fast numerics, by means of appropriate generalizations of two methodologies: 1) The approach based on numerical polar quadrature introduced in references [8, 10], as discussed in Section 5.1, and 2) A suitable generalization, presented in Section 5.2, of the acceleration strategy introduced in reference [8].

5.1. High-order integration. Our strategy for evaluating the integral and differential operators of Section 2 with high-order accuracy for three-dimensional cases results as a generalization of the methodologies introduced in [8, 10]. These algorithms produce the necessary integration and differentiation operators on the basis of *local coordinate charts* (local parametrizations that jointly describe the complete scattering surface) together with *fixed* and *floating* partitions of unity (POU).

Remark 5.1 *In what follows, the subset of a scattering surface that coincides with the image of one of the local parametrizations used will be called a "patch". Thus, for example, using projections onto each one of the three coordinate planes, it is easy to produce six local parametrizations for a sphere and six corresponding patches whose union completely covers the sphere. Complex scatterers require larger number of patches: for example, a complete representation of a full Falcon aircraft was given in [11] on the basis of approximately fifty coordinate patches.*

The fixed POU is a partition of unity subordinated to the open covering of the scattering surface by the set of all patches (see Remark 5.1). Together with the fixed POU, the local parametrizations enable superalgebraically accurate treatment of both, 1) Integration over regions where the integrand is smooth (by means of the two-dimensional trapezoidal rule, see [8, 10]); and 2) Differentiation of smooth surface quantities (see [10]).

The floating POUs, in turn, enable high-order integration of singular interactions. The floating POU functions are pairs of functions of the form $(\eta_{\mathbf{x}}(\mathbf{y}), 1-\eta_{\mathbf{x}}(\mathbf{y}))$ (where $\eta_{\mathbf{x}}$ is a function with a "small" support which equals 1 in a neighborhood of the point $\mathbf{x}$), which can be used to localize the integration problems involving a kernel $H(\mathbf{x},\mathbf{y})$ (which is singular for $\mathbf{y}=\mathbf{x}$) around each observation (target) point $\mathbf{x}$ as indicated by the decomposition

$$\int H(\mathbf{x},\mathbf{y})\psi(\mathbf{y})d\sigma(\mathbf{y}) = \int H(\mathbf{x},\mathbf{y})\psi(\mathbf{y})\eta_{\mathbf{x}}(\mathbf{y})d\sigma(\mathbf{y}) + \int H(\mathbf{x},\mathbf{y})\psi(\mathbf{y})(1-\eta_{\mathbf{x}}(\mathbf{y}))d\sigma(\mathbf{y}). \qquad (38)$$

In detail, the function $\eta_{\mathbf{x}}(\mathbf{y})$ is an infinitely smooth compactly supported windowing function satisfying $\eta_{\mathbf{x}}(\mathbf{y})=1$ for $|\mathbf{x}-\mathbf{y}|<r_0$ and $\eta_{\mathbf{x}}(\mathbf{y})=0$ for $|\mathbf{x}-\mathbf{y}|\geq r_0$. (When used in conjunction with the acceleration methodology described in Sections 5.2.1 and 5.2.2, the parameter r_0 must be chosen as indicated in Remark 5.4.) Clearly, the decomposition (38) enables separate treatment of *singular* and *nonsingular interactions*. The nonsingular interactions term (the second term in equation (38)) involves smooth and periodic quantities which can be integrated accurately by means of the trapezoidal rule. The singular interactions term (the first term in equation (38)) can be evaluated with high-order accuracy by means of a local polar-integration algorithm, provided the kernel singularity of the kernel H is of the order of $\mathcal{O}(|\mathbf{x}-\mathbf{y}|^{-1})$: the Jacobian of the polar coordinate transformation completely regularizes the integrable singularities [8]—in such a way that the trapezoidal rule can once again be used to evaluate the singular contribution with high order accuracy.

Just as in [10], in turn, derivatives of the density μ are performed using fixed POUs, so that only derivatives of smooth and *periodic* functions (that result as products of the integral densities and smooth compactly supported POU functions in parameter space) need to be produced. The derivative of such periodic functions can be computed efficiently and accurately by means of Fast Fourier Transforms and differentiation of rapidly convergent Fourier series.

Finally, the polar integration of integrands that involve exponentials with real arguments, which arise in the kernel of the operator S_{ik_1} with $k_1 > 0$, and which cannot be integrated accurately by means of the trapezoidal-rule in the radial direction, are handled, instead, by means of Newton-Cotes quadrature rules of order seven in the radial direction followed by trapezoidal rule integration in the angular direction, as detailed in reference [10].

Remark 5.2 *Whenever possible, our implementations lump the evaluation of various integral operators whose kernels involve Green's functions with the same wave-number K. If appropriately implemented (re-using components appearing in various kernels, such as distances between integration and observation points, exponentials, etc.), this strategy enables significant reductions in the Green-function evaluation costs per pair of observation-integration points.*

In view of the decompositions put forth in Section 3, the high-order methods mentioned above for differentiation and evaluation of integral operators with kernels of order $\mathcal{O}(|\mathbf{x}-\mathbf{y}|^{-1})$ enable high-order evaluation of all the operators considered in this paper. We put forth two algorithms for the evaluation of the integral operators that enter the ICFIE-R equations (13) (and, in particular, an algorithm for the ICFIE operators): Method I for ICFIE and ICFIE-R, which is based on use of the "integration-by-parts" representation (24) of the operator N_k (and for the ICFIE-R sequential evaluation of the composition $N_k \circ S_{ik_1}$), and Method II for ICFIE-R, which relies on Calderón's formulae (25) for evaluation of the composition $N_k \circ S_{ik_1}$. In detail, using the methodologies described in Section 5.1 for evaluation of individual integral and differential operators, these algorithms proceed as follows.

Algorithm I: Basic ICFIE and ICFIE-R algorithms ($\mathcal{R} = I$ and $\mathcal{R} = S_{ik_1}$, respectively) based on Method I (equations (13) *and* (24)*)*

1. For a given density μ, evaluate $S_{ik_1}\mu$ (ICFIE-R algorithm only);
2. Compute the surface derivatives $\nabla_\Gamma(\mathcal{R}\mu)$ and $\Delta_\Gamma(\mathcal{R}\mu)$ and combine the densities μ, $\nabla_\Gamma(\mathcal{R}\mu)$, and $\Delta_\Gamma(\mathcal{R}\mu)$ (and, for the ICFIE-R algorithm, also $S_{ik_1}\mu$) into an extended vector density $\tilde{\mu}$;
3. Evaluate $(D'_k\mu)$ and, using the "integration by parts" expression (24), evaluate $(N_k\mathcal{R}\mu)$ by applying each of the four operators on the right-hand side of equation (24) to the corresponding components of the vector density $\tilde{\mu}$—lumping common kernel components that enter in the definitions of D'_k and the components of N_k; see Remark 5.2.

Algorithm II: Basic ICFIE-R algorithm based on Method II (equations (13) *and* (25)*)*

(Within each step of this algorithm, evaluation of kernel components are lumped as indicated in Remark 5.2.)

1. For a given density μ compute $S_{ik_1}\mu$ and $D'_{ik_1}\mu$;
2. Similarly, compute $D'_k\mu$ and $(N_k - N_0)(S_{ik_1}\mu)$ (cf. equation (26));
3. Compute $D'_{ik_1}(D'_{ik_1}\mu)$ and $(N_{ik_1} - N_0)(S_{ik_1}\mu)$, and combine the results with the ones in Step 2 to produce the right hand side of equation (25) (cf. equation (26)) and, thus, the left-hand side of equation (13).

The resulting algorithms for evaluation of integral operators can be used, without further additions, to produce high-order iterative solvers for the ICFIE and ICFIE-R integral equations discussed earlier in this text. Significant acceleration of the numerical procedure can be obtained, however, by combining this high-order methodology with the acceleration approach described in the following section.

5.2. Acceleration. In order to enable numerical simulations of high-frequency scattering problems we rely on fast evaluations of the nonsingular interactions (cf. equation (38)) in the discrete version of the boundary integral operators that enter equations (6) and (13). We achieve these fast evaluations by means of a generalization of the acceleration strategy introduced in [8]—which is based on use of certain distributions of monopole and dipole "equivalent sources" on cartesian grids and sparse 3D FFTs, as discussed in Sections 5.2.1 through 5.2.3. As established in [8], depending on the geometrical complexity of the underlying scatterer, this acceleration procedure requires a computational cost of $\mathcal{O}(N^{6/5}\log N)$ to $\mathcal{O}(N^{4/3}\log N)$ operations (with small proportionality constants, cf. Table 9) for evaluation of the discrete integral operators defined by equations (39), where N is the total number of unknowns/discretization points.

As shown in Section 5.2.3, to apply this methodolgy in our context it suffices to provide acceleration methodologies, for "non-adjacent" integral operators of the form

$$(T_K^1\psi)(\mathbf{x}) = \int_\Gamma H_K(\mathbf{x}-\mathbf{y})(1-\eta_{\mathbf{x}}(\mathbf{y}))\psi(\mathbf{y})d\sigma(\mathbf{y}) \tag{39}$$

as well as adequate treatment for "adjacent" integral operators of the form

$$(T_K^2\psi)(\mathbf{x}) = \int_\Gamma H_K(\mathbf{x}-\mathbf{y})\eta_{\mathbf{x}}(\mathbf{y})\psi(\mathbf{y})d\sigma(\mathbf{y}) \quad ,$$

where H_K is one of the following kernels:

$$H_K^1 = G_K \ , \ H_K^2(\mathbf{x},\mathbf{y}) = \frac{\partial G_K(\mathbf{x}-\mathbf{y})}{\partial \mathbf{n}(\mathbf{y})} \ , \ H_K^3(\mathbf{x},\mathbf{y}) = \partial_j G_K(\mathbf{x}-\mathbf{y}) \ , \ H_K^4(\mathbf{x},\mathbf{y}) = \partial_j \frac{\partial G_K(\mathbf{x}-\mathbf{y})}{\partial \mathbf{n}(\mathbf{y})}.$$

Here $\partial_j = \partial/\partial x_j$ for $j = 1, 2, 3$, and $K = k$ or $K = ik_1$ (see Section 2.4). The acceleration algorithms we use for these kernels are described in Sections 5.2.1 and 5.2.2 below.

Remark 5.3 *Note that the kernels H_K^j with $j = 3, 4$ are not weakly singular (they are singular and hyper-singular, respectively). Accordingly, the evaluation of the associated* adjacent *integral operators requires special treatment; see Sections 5.2.3.*

5.2.1. Acceleration of integral operators T_K^1 with kernels H_K^1 and H_K^2 . Our method of acceleration for the integral operators with kernels H_K^1 and H_K^2 is a direct extension of the acceleration method introduced in reference [8] to the case in which the wavenumber may be imaginary. The method [8] relies on a partition of a rectangular parallelepiped C circumscribing the scatterer into $L_1 \cdot L_2 \cdot L_3$ identical cubic cells c_i that do not admit inner acoustic resonances: the parameters are selected in such a way that the real number $-K^2$ is not a Dirichlet eigenvalue of the the Laplace operator in the domain c_i. (Clearly, in the case $K = ik_1$ with $k_1 \geq 0$ this condition is satisfied for cubic cells c_i of any size.) The main elements in this acceleration algorithm are sets of "equivalent sources" which can be used to represent accurately, in large regions of space, the fields produced by the "true" surface sources contained in each cell c_i. As prescribed in [8], the equivalent sources that represent the fields generated by true sources contained in c_i are located on two-dimensional

Cartesian meshes Π_i^ℓ contained on circular neighborhoods (with radii slightly larger than half the diameter of c_i) of pairs of opposing faces of the cells c_i. Thus, the contributions to the discrete integral operator from discretization points contained in c_i are approximated, with high order accuracy, by a number M^{eq} of equivalent sources placed on Π_i^ℓ—for all points in space non-adjacent to c_i, and for $\ell = 1, 2, 3$; see [8]. The precise concept of adjacency we use (namely, two cells c_i are adjacent if and only if they share a face, an edge or a vertex) guarantees that the approximation used for a cell c_i is valid, with exponentially small errors, in the complement of the union of all cells c_j adjacent to c_i. Clearly, the union of c_i and all of the 26 cells c_j adjacent to it constitute a cubic region of side equal to the triple of the side of c_i; in what follows, the boundary of the triple-size cubic region is denoted by $\mathcal{S}_i$. Further, for each ℓ we let $\Pi^\ell = \bigcup_i \Pi_i^\ell$; note that Π^ℓ is a set of points on a Cartesian grid contained in a union of L_ℓ equispaced planes parallel to the plane $x_\ell = 0$.

Equivalent sources and FFTs. At each point in Π_i^ℓ one acoustic monopole $\xi_{i,j}^{(m)\ell}\, G_K(\mathbf{x} - \mathbf{x}_{i,j}^\ell)$ and one acoustic dipole $\xi_{i,j}^{(d)\ell}\, \partial G_K(\mathbf{x} - \mathbf{x}_{i,j}^\ell)/\partial x_\ell$ ($j = 1, \ldots, M^{eq}/2$) are placed for a total of M^{eq} equivalent sources on Π_i^ℓ. The fields $\psi^{c_i,true}$ radiated by the c_i-true sources (that is, all surface sources contained in c_i) are approximated by fields $\psi^{c_i,eq}$ radiated by the c_i-equivalent sources, that is, by the expression

$$\psi^{c_i,eq}(\mathbf{x}) = \sum_{j=1}^{\frac{1}{2}M^{eq}} \left(\xi_{i,j}^{(m)\ell}\, G_K(\mathbf{x} - \mathbf{x}_{i,j}^\ell) + \xi_{i,j}^{(d)\ell} \frac{\partial G_K(\mathbf{x} - \mathbf{x}_{i,j}^\ell)}{\partial x_\ell} \right). \tag{40}$$

For each ℓ and for an adequately chosen number M^{eq} of equivalent sources supported on Π_i^ℓ, the unknown monopole and dipole intensities $\xi_{i,j}^{(m)l}$ and $\xi_{i,j}^{(d)l}$ in equation (40) are chosen so as to minimize, in the mean-square norm, the array of differences $(\psi^{c_i,eq}(\mathbf{x}) - \psi^{c_i,true}(\mathbf{x}))$ for $\mathbf{x}$ varying over a number n^{coll} of adequately selected collocation points on $\mathcal{S}_i$. Hence, for each ℓ, the intensities in (40) are obtained in practice as the least-squares solution of an overdetermined linear system $\mathbf{A}\xi = \mathbf{b}$ where $\mathbf{A}$ is an $n^{coll} \times M^{eq}$ matrix. As in [8], our algorithm exploits certain symmetries in order to reduce by a factor of eight the computational cost associated with the solution of these least-square problems.

Since for a given ℓ the circular regions Π_i^ℓ are not pairwise disjoint, it is necessary to combine equivalent source intensities for sources supported at a given point $\mathbf{x}'$ that corresponds to two different cells, say, c_r and c_s for which $\mathbf{x}' = \mathbf{x}_{r,p}^\ell = \mathbf{x}_{s,q}^\ell$ for some integers p and q. We thus define the quantities

$$\psi^{(*)\ell}(\mathbf{x}) = \sum_{\mathbf{x}' \in \Pi^\ell} \left(\xi_{\mathbf{x}'}^{(m)\ell} G_K(\mathbf{x} - \mathbf{x}') + \xi_{\mathbf{x}'}^{(d)\ell} \frac{\partial G_K(\mathbf{x} - \mathbf{x}')}{\partial x'_\ell} \right) \tag{41}$$

where $\xi_{\mathbf{x}'}^{(m)\ell}$ and $\xi_{\mathbf{x}'}^{(d)\ell}$ denote the sum of all intensities of equivalent sources located at a point $\mathbf{x}' \in \Pi^\ell$:

$$\xi_{\mathbf{x}'}^{(m)\ell} = \sum_{\mathbf{x}_{i,j}^\ell = \mathbf{x}'} \xi_{i,j}^{(m)\ell} \quad \xi_{\mathbf{x}'}^{(d)\ell} = \sum_{\mathbf{x}_{i,j}^\ell = \mathbf{x}'} \xi_{i,j}^{(d)\ell}.$$

Correction step. Clearly, the sum $\psi^{(na,eq)\ell}(\mathbf{x})$ of the values at the point $\mathbf{x} \in \Gamma$ of all fields arising from equivalent sources nonadjacent to c_i can be obtained by subtracting from $\psi^{(*)\ell}(\mathbf{x})$ the field arising at $\mathbf{x}$ from equivalent sources located within $\mathcal{S}_i$, where i is the index for which $\mathbf{x} \in c_i$. Since the quantities $\psi^{(*)\ell}(\mathbf{x})$ are exact convolutions on Cartesian grids, they can be

evaluated accurately and efficiently by means of three-dimensional Fast Fourier Transforms. The "corrections" necessary to produce $\psi^{(na,eq)\ell}(\mathbf{x})$ from $\psi^{(*)\ell}(\mathbf{x})$ can also be evaluated efficiently, by means of three-dimensional FFTs, since they only involve small three-dimensional convolutions (see Remark 5.4). Once completed for $\ell = 1, 2, 3$, this overall procedure results in accurate values, on a mesh that samples the boundaries of all cells c_i, of the fields arising from all true sources contained in all cells c_j not adjacent to c_i.

Remark 5.4 *In order to confine the* correction step *under consideration to domains contained in individual regions $\mathcal{S}_i$, the value of the parameter r_0 that determines the size of the supports of the functions $\eta_{\mathbf{x}}$ (see Section 5.1) is taken to be sufficently small, so that the functions $\eta_{\mathbf{x}}$ vanish outside $\mathcal{S}_i$ for all $\mathbf{x}$ in the cell c_i. (Note in these regards that the fields $\psi^{(na,eq)\ell}(\mathbf{x})$ are approximations of integrals over the "large" region $\Gamma \setminus \mathcal{S}_i$.)*

In order to obtain approximations of the nonadjacent interactions $\psi^{(na,true)}(\mathbf{x})$ (that is, the fields generated at $\mathbf{x}$ by the true discrete surface sources contained outside $\mathcal{S}_i$) at surface points $\mathbf{x} \in \Gamma \cap c_i$, the algorithm employs solutions to the Helmholtz equation within c_i, with Dirichlet boundary conditions given by $\psi^{(na,eq)\ell}$, $\ell = 1, 2, 3$. These Dirichlet problems can be solved uniquely (in view of our assumption that K is not a resonant frequency), and thus the good approximation properties of the nonadjacent interactions on the boundary of each cell c_i translate into good approximations for the nonadjacent interactions on the surface Γ. Following [8], our algorithm produces the needed solutions of Dirichlet problems by means of approximations of the form

$$P(\mathbf{x}) = \sum_{j=1}^{n^w} \gamma^j \exp(iK\mathbf{u}_j \cdot \mathbf{x}), \tag{42}$$

valid within c_i (in terms of plane wave solutions of the Helmholtz equation), for the field $\psi^{(na,true)}$. Here $\mathbf{u}_j$ are unit vectors that adequately sample the surface of the unit sphere, and the coefficients γ^j are obtained in such a way that the relation $P(\mathbf{x}) = \psi^{(na,true)}(\mathbf{x})$ is satisfied, in the least-squares sense, for all $\mathbf{x}$ in an adequately chosen collocation mesh on the cubic surface $\mathcal{S}_i$ (see [8] for details). Notice that, in the case $K = ik_1$, $k_1 \geq 0$, the exponent in equation (42) is real and less than or equal to zero: for purely imaginary wavenumbers the corresponding exponentials are not oscillatory.

Adjacent interactions. Having evaluated, by means of FFTs and plane wave expansions, accurate approximations of the surface values of the field $\psi^{(na,true)}(\mathbf{x})$ produced by the non-adjacent surface sources (for all discretization points $\mathbf{x} \in \Gamma$), surface values of the *total field* are then obtained by direct addition of necessary singular and non-singular adjacent surface sources, as indicated in [8]. Briefly, the fields that need to be added to (the approximations just obtained for) the field $\psi^{(na,true)}(\mathbf{x})$ (for a point $\mathbf{x} \in \Gamma$) include (i) Adjacent regular sources, that is, trapezoidal-rule contributions to the integral operator from sources lying outside the support of the floating POU $\eta_{\mathbf{x}}$ (see Section 5.1) but inside $\mathcal{S}_i$ (none of which are included in $\psi^{(na,true)}(\mathbf{x})$), and (ii) Adjacent singular sources, that is, the local contributions to the integral operator given by the first term in equation (38). Note that, in the cases considered in this section, the contributions in point (ii) are evaluated by a direct application of the singular-integration portion of the algorithm described in Section 5.1.

5.2.2. Acceleration of integral operators with kernels H_K^3 and H_K^4. An acceleration method for integral operators of the form (39) with kernels H_K^3 and H_K^4 results as a generalization of the algorithm described in the previous section. Indeed, direct differentiation of the plane wave

expansion (42) with respect to x_j readily produces the derivatives $\partial_j \psi^{(na,true)}$ of the field arising from non-adjacent sources. Since the supports of the functions $\eta_{\mathbf{x}}$ vanish outside $\mathcal{S}_i$ for all $\mathbf{x}$ in the cell c_i (cf. Remark 5.4), no contributions arise from the function $1 - \eta_{\mathbf{x}}$ in the differentiation of the plane wave expansion (42) with respect to x_j: outside $\mathcal{S}_i$ we have $1 - \eta_{\mathbf{x}} = 1$. As in the last paragraph of the previous section, the total field is produced by addition of derivatives of fields arising from non-singular and singular adjacent sources. The former (cf. point (i) in the last paragraph of the last section) can be easily obtained by differentiation of the Green's function and direct addition of the corresponding contributions to the trapezoidal rule integral. The latter (cf. point (ii) in the previous section), in contrast, cannot be evaluated through direct differentiation. Instead, as indicated in Section 5.1, evaluation of the adjacent-singular differentiated terms proceeds by exploiting the representations presented in Section 3 and use of local polar integrations, as discussed in Section 5.2.3.

5.2.3. Accelerated high-order evaluation of the ICFIE and ICFIE-R matrix-vector products. The methodology presented in Sections 5.2.1 and 5.2.2 enables fast, high-order evaluation of both the ICFIE and ICFIE-R operators—as described in what follows.

Acceleration of the ICFIE operator (6)**:** For a given density μ, an accelerated evaluator for the operator D'_k (and, indeed, more generally, for the operator D'_K with $K = k$ or $K = ik_1$) can be obtained through consideration of the splitting

$$\begin{aligned} \int_\Gamma \frac{\partial G_K(\mathbf{x}-\mathbf{y})}{\partial \mathbf{n}(\mathbf{x})} \mu(\mathbf{y}) d\sigma(\mathbf{y}) &= \int_\Gamma \frac{\partial G_K(\mathbf{x}-\mathbf{y})}{\partial \mathbf{n}(\mathbf{x})} \eta_{\mathbf{x}}(\mathbf{y}) \mu(\mathbf{y}) d\sigma(\mathbf{y}) \\ &+ \sum_{j=1}^{3} \mathbf{n}_j(\mathbf{x}) \int_\Gamma \partial_j G_K(\mathbf{x}-\mathbf{y})(1-\eta_{\mathbf{x}}(\mathbf{y})) \mu(\mathbf{y}) d\sigma(\mathbf{y}) \end{aligned} \tag{43}$$

by using the corresponding accelerated algorithm presented in Section 5.2.1 for the first term on the right-hand side of equation (43), together with the algorithm described in Section 5.2.2 for operators with kernel H^3_K ($j = 1, 2, 3$) for the second operator on the right-hand side of equation (43).

To obtain an accelerated evaluator for the operator N_k, in turn, we rely on equation (24), which reduces this problem to evaluation of a) Single-layer operators for four surface densities ψ (namely $\psi = \Delta_\Gamma \mu$, and $\psi = \mu \mathbf{n}_j$, $j = 1, 2, 3$), b) Double-layer operators (that is, operator with kernel H^2_K for $K = k$) for two densities ψ (namely, the two components of the surface gradient $\nabla_\Gamma \mu$, and, finally, c) The second integral operator in equation (24). The operators in points a) and b) can be evaluated directly by means of the approach based on acceleration of non-adjacent interactions and polar/trapezoidal integration of adjacent interactions described in Section 5.2.1.

The evaluation of operators in point c) can also be accelerated by a similar approach. Indeed, the second integral operator in equation (24) can once again be split by means of the floating POU $\eta_{\mathbf{x}}$. The singular term can then be evaluated with high order accuracy by means of the polar integration approach, in view of the $1/|\mathbf{x}-\mathbf{y}|$ singular character of its kernel $\nabla^{\mathbf{y}} G_k(\mathbf{x}-\mathbf{y})(1 - \mathbf{n}(\mathbf{x}) \cdot \mathbf{n}(\mathbf{y}))$. The remainder of this operator, finally, can be accelerated by means of the approach described in Section 5.2.2 for the kernel H^3_K, by first replacing $\nabla^{\mathbf{y}}$ by $-\nabla^{\mathbf{x}}$ and reducing the problem to four integrals, one associated with the term "1" in the parenthesis $(1 - \mathbf{n}(\mathbf{x}) \cdot \mathbf{n}(\mathbf{y}))$, and the other three arising from each one of the components of the normal $\mathbf{n}(\mathbf{y})$, with $\mathbf{n}(\mathbf{x})$ placed outside of the integral sign. All of the resulting operators can be evaluated by means of the approach based on acceleration of non-adjacent interactions described for the operator H^3_K in Section 5.2.2.

Acceleration of the ICFIE-R operator (13)**:** In order to accelerate the evaluation of the left-hand-side operator in equation (13) we use accelerated algorithms for evaluation of D'_k and $N_k \circ \mathcal{R}$. An accelerated algorithm for the former was presented above in this section (see equation (43)). In what follows we present two different approaches, Method I and Method II, leading to accelerated evaluation of the composite operator $N_k \circ \mathcal{R}$.

Method I is based, simply, on sequential accelerated evaluation of the operators S_{ik_1} and N_k. Methods for accelerated evaluation of these two operators have already been described: the first one in Section 5.2.1 (since S_{ik_1} is an operator with kernel H^1_K with $K = ik_1$), and the second one in the paragraph entitled "Acceleration of the ICFIE operator" above in this section.

Method II, in turn, relies on the Calderón-like formula (25) together with the accelerated algorithm described above in this section for the operators D'_K (this time, with $K = ik_1$) together with a methodology, which does not require evaluation of either $N_k\psi$ or $N_{ik_1}\psi$, for application of the difference $N_k - N_{ik_1}$ to $\psi = S_{ik_1}\mu$. The algorithm proceeds by first producing ψ by means of the acceleration strategies presented in Section 5.2.1 for operators with kernels $H^1_{ik_1}$ and then applying to ψ the various operators on the right-hand-side of the equation

$$\begin{aligned}((N_k - N_{ik_1})\psi)(\mathbf{x}) &= \int_\Gamma H^5_k(\mathbf{x},\mathbf{y})\eta_{\mathbf{x}}(\mathbf{y})\psi(\mathbf{y})d\sigma(\mathbf{y}) - \int_\Gamma H^5_{ik_1}(\mathbf{x},\mathbf{y})\eta_{\mathbf{x}}(\mathbf{y})\psi(\mathbf{y})d\sigma(\mathbf{y}) \\ &+ \sum_{j=1}^{3} \mathbf{n}_j(\mathbf{x}) \left(\int_\Gamma H^4_k(\mathbf{x},\mathbf{y})(1-\eta_{\mathbf{x}}(\mathbf{y}))\psi(\mathbf{y})d\sigma(\mathbf{y}) - \int_\Gamma H^4_{ik_1}(\mathbf{x},\mathbf{y})(1-\eta_{\mathbf{x}}(\mathbf{y}))\psi(\mathbf{y})d\sigma(\mathbf{y}) \right)\end{aligned} \tag{44}$$

where

$$H^5_K(\mathbf{x},\mathbf{y}) = \frac{\partial^2(G_K(\mathbf{x}-\mathbf{y}) - G_0(\mathbf{x}-\mathbf{y}))}{\partial\mathbf{n}(\mathbf{x})\partial\mathbf{n}(\mathbf{y})} \qquad \text{for } K = k \quad \text{or} \quad K = ik_1.$$

It is easy to check that the kernels of the first two terms of the right-hand side of this equation (the "singular interaction" terms) are weakly singular of order $\mathcal{O}(|\mathbf{x}-\mathbf{y}|^{-1})$. These integrals can therefore be evaluated by means of the polar-integration methodology described in Section 5.1 which, in particular, calls for evaluation of the radial integrals by means of the trapezoidal rule for the first of these two kernels, and use of the Newton Cotes formula of order seven for the second one. The last two terms in equation (44), finally, can be produced by means of the acceleration strategies presented in Section 5.2.2 for operators with kernels H^4_K with $K = k$ and $K = ik_1$, respectively.

Each one of the two corresponding approaches described above for evaluation of the operator $N_k \circ S_{ik_1}$ gives rise to a solver for the ICFIE-R equation (13). Along the lines of the Algorithms I and II described in Section 5.1 but using here the acceleration methods introduced above in the present Section 5.2, in what follows we present the major steps of each of two accelerated algorithms for the evaluation of the ICFIE and ICFIE-R operators.

Algorithm III: Accelerated ICFIE and ICFIE-R algorithms ($\mathcal{R} = I$ and $\mathcal{R} = S_{ik_1}$, respectively) based on Method I (equations (13) and (24))

1. For a given density μ, evaluate $S_{ik_1}\mu$ according to the strategy presented in Section 5.2.1 for operators with kernel H^1_K with $K = ik_1$ (ICFIE-R algorithm only);

2. Compute the surface derivatives $\nabla_\Gamma(\mathcal{R}\mu)$ and $\Delta_\Gamma(\mathcal{R}\mu)$ and combine the densities μ, $\nabla_\Gamma(\mathcal{R}\mu)$, and $\Delta_\Gamma(\mathcal{R}\mu)$ (and, for the ICFIE-R algorithm, also $S_{ik_1}\mu$) into an extended vector density $\tilde{\mu}$;

3. Using the strategy for the evaluation of the operator N_k presented in the paragraph entitled "Acceleration of the ICFIE operator", apply the operators D'_k and N_k to the corresponding components of the vector density $\tilde{\mu}$—lumping common kernel components that enter in the definitions of H_k^1, H_k^2 and H_k^3; see Remark 5.2.

Algorithm IV: Accelerated ICFIE-R algorithm based on Method II (equations (13) and (25))

(Within each step of this algorithm, evaluation of kernel components are lumped as indicated in Remark 5.2.)

1. For a given density μ compute $S_{ik_1}\mu$ and $D'_{ik_1}\mu$ using one accelerated evaluation of operators with kernels H_K^1 and H_K^3 with $K = ik_1$;

2. Compute $D'_k\mu$ and $N_k(S_{ik_1}\mu)$ by means of one accelerated evaluation of operators with kernels H_K^3 and H_K^4 with $K = k$ and local singular evaluations of operators with kernels H_K^5 with $K = k$;

3. Compute $D'_{ik_1}(D'_{ik_1}\mu)$ and $N_{ik_1}(S_{ik_1}\mu)$, by means of an accelerated evaluation of operators with kernels H_K^3 and H_K^4 with $K = ik_1$ and local singular evaluations of operators with kernels H_K^5 with $K = ik_1$; finally, combine the results with the ones in Step 2 to produce the right hand side of equation (25), and, thus, the left-hand side of equation (13).

Remark 5.5 *From the descriptions of Methods I and II we see that, in view of the strategy based on simultaneous evaluation of operators with kernels of a given wavenumber, Method I requires evaluation of kernels for two different wavenumbers: $K = ik_1$ (point 1) and $K = k$ (point 3). Method II, in turn, requires evaluation of kernels for three different wavenumbers, namely $K = ik_1$ (point 1), $K = k$ (point 2) and once again $K = ik_1$ (point 3). Since the main difference between the computational times required by Methods I and II arise mainly from the corresponding kernel evaluations for the singular-interactions portion of the integration process described in Section 5.1 (see Table 9), Method II requires* 1.5 *times the computing time required by Method I—a fact that is clearly supported by comparison of the time-per-iteration data reported in Table 7. Similarly, it can be verified that Method II requires approximately* 1.6 *times as much memory as Method I—since the memory requirements of Methods I and II arise mainly from the storage required by the corresponding numbers of Fourier transforms of densities and kernels that need to be kept in memory. Although Method II requires higher computational and memory costs than Method I, the former approach does offer some advantages: Method II does not entail numerical differentiations and thus 1) It is more accurate than Method I (cf. Table 7), and 2) It can be incorporated more easily into other contexts, possibly including non-smooth surfaces as well as other Galerkin or Nyström boundary integral methods.*

6 Numerical Results

In this section we present a variety of numerical results that demonstrate the properties of both the classical and regularized combined field integral equations (6) and (13). The results presented in this section for the new regularized equations were obtained by means of regularizing operators $\mathcal{R} = S_{ik_1}$ with parameter values k_1 and η as specified in Section 2. For the ICFIE formulations we used $\eta = 1/k$ as prescribed in [24]. Solutions of the various integral equations were produced by means of the fully complex version of the iterative solver GMRES [30] with residual tolerance as

specified in each case. Amongst other statistics, the various tables in this section present values of the maximum error

$$\varepsilon_\infty = \max|u_\infty^{s,\mathrm{num}}(\hat{\mathbf{x}}) - u_\infty^{s,\mathrm{ref}}(\hat{\mathbf{x}})| \tag{45}$$

in the numerical values of the far-field

$$u^s(\mathbf{x}) = \frac{e^{ik|\mathbf{x}|}}{|\mathbf{x}|^{(d-1)/2}} \left(u_\infty^s(\hat{\mathbf{x}}) + \mathcal{O}\left(\frac{1}{|\mathbf{x}|}\right)\right), \ |\mathbf{x}| \to \infty \tag{46}$$

($d = 2$, 3), over all scattering directions $\hat{\mathbf{x}} = \mathbf{x}/|\mathbf{x}|$. The maximum far-field errors in the numerical solutions $u_\infty^{s,\mathrm{num}}$ were evaluated through comparison with adequately accurate reference solutions $u_\infty^{s,\mathrm{ref}}$ over a sufficiently fine angular mesh. The needed reference quantities $u_\infty^{s,\mathrm{ref}}$ were produced through evaluation of exact solutions, when available, or by means of numerical solution with sufficiently fine discretizations, otherwise; see Sections 6.1 and 6.2 for details. All of the numerical results presented in this paper were obtained by means of C++ numerical implementations of our algorithms, and using the gcc compiler. The two-dimensional results (Section 6.1) were produced in a single core of a 2.4 GHz MacBook Pro laptop with 2 GB of RAM. The three-dimensional results (Section 6.2) were produced in a single core of a 2.27 GHz Intel (R) Xeon multicore processor with 24 GB of RAM under the GNU/Linux operating system and using the GNU/gcc compiler, the PETSC 3.0 library for the fully complex implementation of GMRES, and the FFTW3 library for evaluation of FFTs. Throughout this section, the "relative residual" at the m-th iteration in a GMRES iterative solutions is defined as the quotient of the residual after m iterations by the residual after the first iteration.

6.1. Two-dimensional test cases. Table 1 presents results for a simple multiple-reflection two-dimensional configuration: the kite-shaped scatterer parametrized by the equation $x(t) = (\cos t + 0.65\cos 2t - 0.65, 1.5\sin t)$ [23] under plane-wave incidence in the direction $(\frac{\sqrt{2}}{2}, \frac{\sqrt{2}}{2})$. Table 1 displays the number of iterations (iter.) required by the GMRES solver to a relative residual of 10^{-8} for discretizations corresponding to 8 and 12 points per wavelength, and for frequencies in the medium to high-frequency range, $k = 2^i, i = 3, \ldots, 8$, corresponding to acoustical sizes ranging from 2.5λ to 81.6λ. The column "N" in the table displays the numbers of unknowns (equal to $2n$, see Section 4) used in each case. In this case, the needed reference quantities $u_\infty^{s,\mathrm{ref}}$ were produced by means of numerical solutions of the classical ICFIE formulation (6) with sufficiently fine discretizations.

Clearly, the regularized equations require significantly smaller numbers of GMRES iterations, with improvement factors that grow rapidly as the frequency increases. As demonstrated by Table 1, further, in the present two-dimensional case, a ICFIE-R matrix-vector product is on average only 1.1 times more expensive (in terms of computing time) than the corresponding matrix-vector product for the ICFIE formulation at the same level of discretization. As a result, the overall computing times required by the ICFIE-R formulation are quite favorable for all frequency regimes considered: approximately one order of magnitude shorter, for the same level of accuracy in the solution, than those required by the ICFIE approach.

The ICFIE-R computing-time improvements demonstrated in Table 1 relate to the spectral properties characterized in Theorem 2.1. A different interpretation of the implications of this theorem emerges from consideration Table 1 under a different perspective: while, for each frequency, the classical ICFIE formulation requires increasing numbers of iterations as the discretization of a problems are refined, the regularized ICFIE-R formulations do not—as expected for the discretization of a second kind integral equation. Figure 1, finally, demonstrates the spectral properties of the ICFIE-R operators with $\mathcal{R} = S_{ik}$ for the kite and circular geometries, $k = 128$ and $N = 1436$.

Size	N	ICFIE			ICFIE-R			
		Iter.	Time	Time/Iter	Iter.	Time	Time/Iter	ε_∞
2.5λ	64	103	12.36 s	0.12 s	19	2.47 s	0.13 s	7.2×10^{-5}
2.5λ	96	161	27.37 s	0.17 s	19	3.42 s	0.18 s	1.7×10^{-8}
5.1λ	128	125	33.75 s	0.27 s	20	5.6 s	0.28 s	2.2×10^{-5}
5.1λ	192	191	1.53 m	0.48 s	20	10.12 s	0.51 s	1.4×10^{-8}
10.2λ	256	145	2.07 m	0.86 s	21	0.3 m	0.88 s	1.0×10^{-5}
10.2λ	384	213	6.28 m	1.77 s	20	0.61 m	1.82 s	1.9×10^{-8}
20.4λ	512	156	8.03 m	3.09 s	21	1.1 m	3.15 s	2.0×10^{-5}
20.4λ	768	212	24.10 m	6.82 s	21	2.45 m	7 s	3.0×10^{-8}
40.8λ	1024	167	33.54 m	12.05 s	22	4.53 m	12.35 s	1.9×10^{-5}
40.8λ	1536	209	1.57h	27.00 s	22	10.11 m	27.56 s	2.0×10^{-8}
$81.6\ \lambda$	2048	200	2.66 h	48 s	26	0.36 h	49 s	2.0×10^{-5}
$81.6\ \lambda$	3072	306	9.09 h	107 s	26	0.81 h	112s	2.5×10^{-8}

Table 1: Kite-shaped scatterer defined in the text. Plane wave incidence

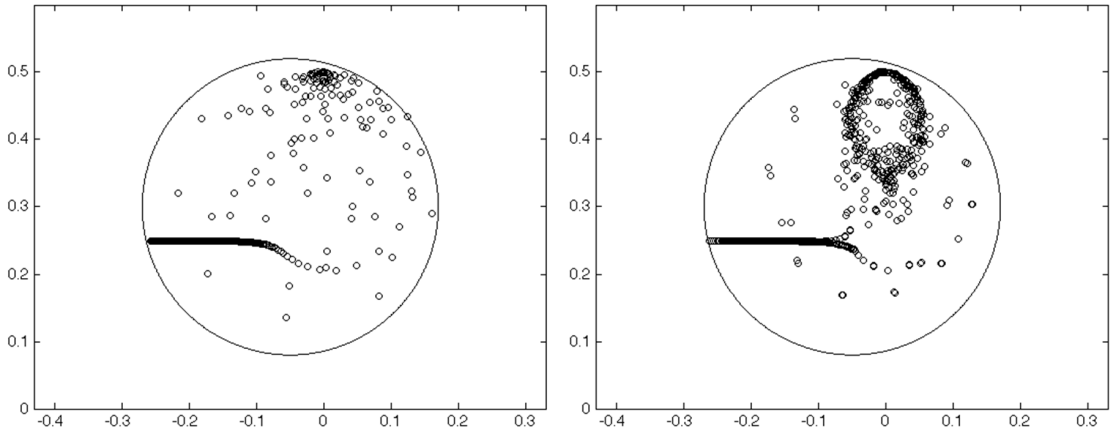

Figure 1: Computed eigenvalue distribution of the ICFIE-R operators (13) with $\mathcal{R} = S_{ik}$ for circle (left) and kite (right) for $k = 128$. We used $N = 1436$ discretization points. In each case the eigenvalues are enclosed by a circle, centered at (-0.05, 0.3) and with radius $R = 0.22$ ($\frac{R}{|c|} = 0.65$), which is well bounded away from zero and infinity.

(The eigenvalues presented in this figure were obtained by explicitly building the matrices arising from the ICFIE-R formulations and evaluating the corresponding eigenvalues by means of the "eig" MATLAB function.) We note that in both cases the eigenvalues are enclosed by the circle centered at $c = (-0.05, 0.3)$ ($|c| \approx 0.3$) with radius $R = 0.22$, for which $\frac{R}{|c|} = 0.72$. Such favorable eigenvalue distribution (contained in circles bounded away from zero and infinity) are known to lead to super-linear convergence of the GMRES iterative solver [30].

6.2. Three-dimensional test cases. In spite of the high-order convergence inherent in the solvers presented in Section 5.1, the ability of these algorithms to effectively produce accurate solutions for high frequency problems is limited by their $\mathcal{O}(N^2)$ computational cost. As illustrated in Section 6.2.2, this difficulty can be successfully addressed by means of the FFT acceleration techniques described in Section 5.2 (cf., in particular, Table 9). For sufficiently low frequencies, however, the unaccelerated algorithm are generally more efficient—since, for such cases, the over-

head associated with the acceleration method outweighs its benefits. In Sections 6.2.1 and 6.2.2 we thus present solutions produced by unaccelerated and accelerated versions of our solvers, for low and high frequencies, respectively. These results show that low iteration numbers, fast numerics and high accuracies result from the combination of integral formulations and solvers presented in this paper—for low and high frequencies alike.

In the next two sections we thus present a variety of numerical results for three geometries (a sphere, an ellipsoid and the bean-shaped scatterer described in [8] and depicted on the right panel of Table 4) for a wide range of frequencies. Our numerical tables include far-field errors resulting from the various algorithms, with discretizations and GMRES residual tolerances as specified in each case. In each table, the column labeled "Patches" presents the values of the expression $p \times n_x \times n_y$, where p denotes the number of patches used in the corresponding run, and where n_x and n_y denote the numbers of discretization points used along each coordinate direction in each patch. (Given the simplicity of the geometries considered in this paper, for each run a fixed number $n_x \times n_y$ of patch discretization points is used for all patches.) The column labeled "N", in turn, displays the overall number of unknowns used in each run. Note that generally $N < p \cdot n_x \cdot n_y$, since only the patch discretization points for which the correponding fixed POU function (introduced in Section 5.1) does not vanish are taken to support unknown values of the surface density. The numerical errors quoted were evaluated through comparison with reference solutions $u_\infty^{s,\mathrm{ref}}$ obtained from the Mie series in the case of spherical scatterers, and, for non-spherical scatterers, by means of equation ICFIE-R (13) with $\mathcal{R} = S_0$, using Method II of Section 5.2.3 (which does not require evaluation of surface derivatives of the unknown density), with fine discretizations and small relative GMRES residuals.

6.2.1. Unaccelerated solvers. The first table in this section, Table 2, demonstrates the high-order character of our algorithms: doubling the overall discretization density (which is achieved by halving the meshsize in each patch) consistently results in accuracy improvements by two orders of magnitude. In detail, this table displays the far-field error ε_∞ produced by increasingly refined discretizations of a sphere of radius 2.7λ using the ICFIE-R formulation (13) with $\mathcal{R} = S_0$ under a plane-wave incident field u^{inc}. The columns labeled "ε_∞ (Algorithm I)" and "ε_∞ (Algorithm II)" display the ε_∞ errors that resulted from use of the Algorithms I and II presented in Section 5.1, with relative GMRES tolerances of 10^{-4} for the first two discretizations, and GMRES tolerances of 10^{-6} and 10^{-8} for the last two cases, respectively. The acoustical size of the problem and the discretizations used for the sound-hard problem in this table are identical to those utilized for the sound-soft case considered in Table IV of reference [8], and, indeed, the maximum far-field errors in Table 2 are of the same order as those reported in that reference. We see that for the coarser discretizations considered in Table 2 the errors incurred by numerical differentiation in Algorithm I lead to somewhat larger numbers of iterations to reach a prescribed GMRES tolerance, and they give rise to far-field errors that are up to one order of magnitude larger than those produced by Algorithm II. For the finer discretizations, however, the far-field errors produced by the two algorithms are comparable and the iteration numbers are identical.

Table 3 compares the performance of the classical ICFIE formulation (6) and the regularized ICFIE-R formulation (13) under Algorithm I and Algorithm II. For each discretization the far-field errors arising from the three versions were comparable: of the order 10^{-3} for the coarser discretizations and of the order 10^{-4} for the finer discretizations. The slightly higher computational times that were incurred for the bean-shaped geometries are due to the use of larger overlap between patches—which was found necessary to reach the same level of accuracy as in the sphere and ellipsoid geometries. We see that a matrix-vector product resulted from discretization of the ICFIE-R

Patches	N	Discretization density	ε_∞ (Algorithm I)	ε_∞ (Algorithm II)
$6 \times 17 \times 17$	1,350	3 per λ	1.2×10^{-2}	3.9×10^{-3}
$6 \times 33 \times 33$	5,766	6 per λ	2.4×10^{-4}	3.0×10^{-5}
$6 \times 65 \times 65$	23,790	12 per λ	4.4×10^{-6}	1.2×10^{-6}
$6 \times 129 \times 129$	93,726	24 per λ	7.2×10^{-8}	3.2×10^{-8}

Table 2: Convergence study. Scattering from a sphere of radius equal to 2.7λ, using the ICFIE-R formulation (13) with $\mathcal{R} = S_0$, and in conjunction with two different implementations: Algorithm I and Algorithm II of Section 5.1. For both algorithms, GMRES tolerances of 10^{-4}, 10^{-4}, 10^{-6} and 10^{-8} were imposed for the discretizations containing 1,350, 5,766, 23,790 and 93,726 unknowns, respectively. The Algorithm-I based solver reached the required GMRES tolerances in a total of 24, 17, 19, and 24 GMRES iterations, respectively. The Algorithm-II based solver, in turn, required 19, 16, 19, and 24 iterations, respectively.

Scatterer	N	ICFIE		ICFIE-R Algorithm I		ICFIE-R Algorithm II	
		Time/It.	It./Tot. time	Time/It.	It./Tot. time	Time/It.	It./Tot time
Sphere	2,646	2.56 sec	16/41 sec	3.92 sec	12/47 sec	3.5 sec	10/35 sec
Sphere	5,400	7.77 sec	18/140 sec	11.81 sec	11/130 sec	11.45 sec	11/126 sec
Ellipsoid	2,646	2.60 sec	23/60 sec	4.00 sec	12/48sec	3.5 sec	10/35 sec
Ellipsoid	5,400	7.76 sec	25/194 sec	12.00 sec	12/144 sec	11.4 sec	10/114 sec
Bean	2,646	3.56 sec	25/89 sec	5.00 sec	12/60 sec	5.27 sec	11/58 sec
Bean	5,400	9.74 sec	27/263 sec	14.08 sec	12/169 sec	15.25 sec	12/183 sec

Table 3: Comparisons. Scattering from objects of diameter equal to 5.4λ, plane wave incidence, using the ICFIE formulation (6) with coupling parameter $\eta = 1/k$ and the ICFIE-R formulation (13) and Algorithm I and Algorithm II with $\mathcal{R} = S_{ik/2}$ and $\xi = 1$. The ellipsoid is an elongated ellipsoid of semi-axes $a = 1$, $b = 0.375$ and $c = 0.5$. See commented FOR THE CAPTION OF THE TABLE ABOVE in the tex file.

formulations is at most 1.4 times more computationally expensive than the matrix-vector product for the ICFIE formulation at the same level of discretization. The ICFIE-R runs are noticeably faster than those arising from their classical ICFIE counterparts; as shown in Section 6.2.2, further, even more significant improvement factors in computing times result from the new formulations in high-frequency cases.

Table 4, finally, demonstrates the character of the solvers based on the ICFIE and ICFIE-R formulations with that of a solver based on the new, direct regularized formulation DCFIE-R (see Remark 2.3). (In these cases we used the Algorithm I implementation for the ICFIE-R equation, and a similar algorithm for the DCFIE-R.) As shown in this table, all three equations give rise to equally accurate results, but both the indirect and direct regularized equations converge in significantly smaller numbers of GMRES iterations: using 4,374, 18,150 and 73,926 unknowns corresponding to 6 patches and 27×27, 55×55 and 111×111 points per patch (approximately 9 points per wavelength) the regularized formulations require less than one-third of the number of iterations required by their classical counterparts.

6.2.2. Accelerated solvers. The results presented in this section demonstrate the properties of the accelerated high-frequency implementations, described in Section 5.2, of the classical formulation ICFIE and new regularized formulation ICFIE-R. Each numerical table displays the values of the parameters used, including the number N of unknowns and the parameters associated with the various components of the acceleration algorithm: the numbers M^{eq}, n^{coll} and n^w as well as a common value L for the parameters L_1, L_2 and L_3. The far field errors ε_∞ were computed using either Mie series solutions in the case of spherical scatterers or solutions obtained from fine discretizations

Size	N	ICFIE		ICFIE-R		DCFIE-R	
		Iter.	ε_∞	Iter.	ε_∞	Iter.	ε_∞
2.5λ	4374	31	8.3×10^{-3}	11	5.3×10^{-3}	9	4.0×10^{-3}
5.1λ	18150	37	1.6×10^{-4}	10	1.2×10^{-4}	10	2.1×10^{-4}
10.2λ	73926	41	2.3×10^{-4}	13	3.9×10^{-4}	13	2.6×10^{-4}

Table 4: Left: Scattering by the bean-shaped obstacle depicted on the right panel; plane-wave incidence of direction $(-\frac{\sqrt{3}}{3}, -\frac{\sqrt{3}}{3}, -\frac{\sqrt{3}}{3})$ which gives rise to multiple reflections. Right: Bean-shaped obstacle.

selected as follows: in all Tables in Section 6.2.2 except for Table 5 discretizations correponding to 9 points per wavelength for problems of size less than or equal to 50λ and discretizations using 2,358,774 unknowns for the problems of size 100λ—the latter corresponds to discretizations using 6 points per wavelength, and in Table 5 discretizations correponding to 12 points per wavelength. The computational times and memory usage reported resulted from a C++ numerical implementation of our 3D algorithms on a single core of a GHz Intel (R) Xeon processor with 24 GB of memory. (All of the computatonal times reported in this paper correspond to runs performed on a single processor.) In some of the tables we present two selections of acceleration parameters for each incoming frequency: one selection that leads to faster run-times and another that leads to lower memory usage. For the elongated ellipsoids, the choice that leads to short run-times also leads to very good memory usage. We conclude from the results presented in the tables in this section that, in accordance with [8], the computational cost of one matrix-vector product of size N associated with our accelerated algorithms is $\mathcal{O}(N^\alpha \log N)$ with $6/5 \leq \alpha \leq 4/3$, regardless of the integral equation used.

Table 5 demonstrates the performance of the solvers based on accelerated ICFIE and ICFIE-R algorithms for elongated ellipsoids at moderate to high frequencies. We see that both the classical and regularized equations give rise to equally accurate results, but the regularized equations converge in significantly smaller numbers of GMRES iterations. For the finest discretization in the case $D = 30\lambda$, which corresponds to approximately 9 points per wavelength, for example, the regularized solver reaches the required GMRES residual in less than one-sixth of the number of iterations required by their classical counterpart. Given that, for the problems under consideration, the accelerated regularized formulations are at most 1.6 times more expensive per iteration than the corresponding un-regularized versions, it follows that use of the regularized equations gives rise, in these cases, to reductions in computing times by a factor of approximately four. Furthermore, this table demonstrates that the numbers of iterations required by the second-kind ICFIE-R equations to reach a certain GMRES tolerance is virtually independent of the fineness of the discretization (provided sufficiently fine discretizations are used). This stands in contrast with the performance of the ICFIE-based solvers: as can be seen in Table 5, the ICFIE algorithms require increasing numbers of GMRES iterations as the discretizations are refined.

Table 6 compares the iteration numbers required by the ICFIE-R integral operators based on the regularizer $\mathcal{R} = S_{ik/2}$ with those arising from the classical selection $\mathcal{R} = S_0$ (see [28] and the related discussion in Section 1). For all the configurations we have investigated we have found that, as illustrated in Table 6, the ICFIE-R formulations with $\mathcal{R} = S_{ik/2}$ consistently reach a given residual in fewer iterations than the ICFIE-R formulations with $\mathcal{R} = S_0$—with improvements factors in the number of iterations and computing times that increase significantly as the frequency grows. Among the three geometrical configurations considered in this paper, the benefits that result

Size (D)	N	L	M^{eq}	n^{coll}	n^w	ICFIE				ICFIE-R Algorithm III			
						ε_∞	Mem	Time/It	It/ Tot. time	ε_∞	Mem	Time/It	It/ Tot. time
10.2 λ	23,814	8	6	10	6	3.0×10^{-3}	0.07 Gb	0.92m	53/48.66m	1.5×10^{-3}	0.068 Gb	1.44m	13/18.83m
10.2 λ	54,150	12	6	10	6	2.5×10^{-4}	0.13 Gb	2.27m	87/3.26h	1.2×10^{-4}	0.15 Gb	3.57m	13/46.5m
20.4 λ	96,774	16	6	10	6	1.7×10^{-3}	0.32 Gb	3.55m	57/3.38h	8.2×10^{-4}	0.36 Gb	5.62m	16/1.5h
20.4 λ	218,886	24	6	10	6	3.1×10^{-4}	0.56 Gb	9.63m	99/15.9h	1.4×10^{-4}	0.76 Gb	15.12m	15/3.8h
30 λ	237,606	24	6	10	6	1.2×10^{-3}	0.77 Gb	11.5m	67/12.9h	1.7×10^{-3}	0.85 Gb	17.43m	18/5.23h
30 λ	536,406	36	6	10	6	2.7×10^{-4}	1.3 Gb	28.4m	129/61.1h	2.3×10^{-4}	1.7 Gb	44.6m	18/13.38h

Table 5: Comparison between the ICFIE and ICFIE-R formulations, accelerated computations for ellipsoids of size $D \times D/4 \times D/4$, plane wave normal incidence.

Size	N	L	ICFIE-R, $\mathcal{R} = S_{ik/2}$			ICFIE-R, $\mathcal{R} = S_0$		
			ε_∞	Time/It	It/ Tot. time	ε_∞	Time/It	It/ Tot. time
10.2 λ	23,814	8	6.0×10^{-3}	1.13m	16/18.2m	2.1×10^{-3}	0.85m	25/21.2m
20.4 λ	96,774	16	4.5×10^{-3}	4.94m	21/1.73h	3.4×10^{-3}	4.45m	40/2.97h
30 λ	237,606	24	5.4×10^{-3}	14.98m	24/5.99h	3.6×10^{-3}	13.76m	51/11.7h
40.8 λ	390,150	32	4.3×10^{-3}	23.11m	27/10.4h	3.7×10^{-3}	20.57m	66/22.63h
50 λ	587,814	40	2.3×10^{-3}	40.24m	29/19.45h	3.5×10^{-3}	38.33m	76/48.55h
100 λ	1,500,000	28	6.2×10^{-3}	3.43h	37/127.16h	5.7×10^{-3}	3.17h	137/435.1h

Table 6: Comparison between the performance of the accelerated solvers based on the ICFIE-R formulations with $\mathcal{R} = S_{ik/2}$ and $\mathcal{R} = S_0$ using Algorithm III for the bean-shaped geometry under plane wave incidence of direction $(-\frac{\sqrt{3}}{3}, -\frac{\sqrt{3}}{3}, -\frac{\sqrt{3}}{3})$.

from use of the $\mathcal{R} = S_{ik/2}$ regularizer are most significant for the bean-shaped geometry with plane wave incidence giving rise to multiple reflections. As shown in Table 6, at the highest frequencies (problems of acoustic size of one hundred wavelengths) these improvements amount to savings by a factor of approximately four in computational times over those resulting from the regularizer $\mathcal{R} = S_0$.

Table 7 presents a comparison between the performance of the accelerated solvers based on Algorithms III and IV of Section 5.2. As discussed in Remark 5.5 and demonstrated by the results in Table 7, the solvers based on Algorithm IV, although more accurate for coarser discretizations (Table 7 was produced on the basis of six-points-per-wavelength discretizations), require up to 1.5 times longer computational times and up to 1.6 times higher memory costs than the solvers based on Algorithm III.

Table 8, in turn, presents results of high-frequency scattering experiments for the bean shaped geometry under plane-wave incidence, using the ICFIE-R formulations with $\mathcal{R} = S_{ik/2}$ and approximately 6 discretization points per wavelength. For reference, in the last row of Table 8 we present a result for the Dirichlet case, note the Dirichlet solver requires fewer iterations as well as lower time and memory costs per iteration. The latter difference reflects the computational cost of the regularization technique; the former difference must be attributed to a superior spectral character of the classical formulation [7] that applies to the Dirichlet problem. (The results in the last line of Table 8 were obtained by means of our own, new C++ implementation of the Dirichlet solver described in [8].)

Table 9, presents a discriminated list of the computing costs associated with an application of our accelerated algorithms, and it provides a comparison with the wide-band FMM algorithm [19]. Since the results presented in [19] only concern accelerated evaluations of sums of Green's functions

Size	N	L	M^{eq}	n^{coll}	n^w	ICFIE-R Algorithm III				ICFIE-R Algorithm IV			
						ε_∞	Mem	Time/It	It/ Tot. time	ε_∞	Mem	Time/It	It/ Tot. time
10.2 λ	23,814	6	10	14	10	1.1×10^{-3}	0.11 Gb	1.6m	14/22.42m	2.8×10^{-4}	0.28 Gb	2.65m	12/31.9m
10.2 λ	23,814	8	6	10	6	1.2×10^{-3}	0.16 Gb	0.97m	14/13.63m	2.7×10^{-4}	0.31 Gb	1.44m	12/17.3m
20.4 λ	96,774	10	10	14	10	1.8×10^{-3}	0.50 Gb	6.58m	17/1.87h	4.3×10^{-4}	0.79 Gb	10.24m	15/2.56h
20.4 λ	96,774	16	6	10	6	1.8×10^{-3}	0.55 Gb	4.4m	17/1.25h	4.2×10^{-4}	0.94 Gb	6.48m	15/1.62h
30 λ	237,606	14	10	14	10	2.6×10^{-3}	1.0 Gb	18.66m	18/5.6h	4.7×10^{-4}	1.6 Gb	27.17m	17/7.70h
30 λ	237,606	24	6	10	6	2.5×10^{-3}	1.3 Gb	13.22m	18/3.96h	4.7×10^{-4}	1.9 Gb	18.98m	17/5.38h
40.8 λ	390,150	20	10	14	10	2.2×10^{-3}	2.0 Gb	29.55m	20/9.8h	5.2×10^{-4}	3.0 Gb	46.36m	19/14.68h
40.8 λ	390,150	32	6	10	6	2.1×10^{-3}	2.4 Gb	21.35m	20/7.11h	5.1×10^{-4}	3.5 Gb	32.84m	19/10.4h
50 λ	587,814	24	10	14	10	2.4×10^{-3}	2.9 Gb	49.4m	22/18.1h	4.9×10^{-4}	4.6 Gb	1.31h	20/26.16h
50 λ	587,814	40	6	10	6	2.4×10^{-3}	3.8 Gb	36.09m	22/13.23h	4.8×10^{-4}	5.5 Gb	54.24m	20/18.08h

Table 7: Comparison between the accelerated solvers based on ICFIE-R formulations and Algorithm III and Algorithm IV, spherical scatterers under plane wave normal incidence.

Size	N	L	M^{eq}	n^{coll}	n^w	ε_∞	Mem	Time/It	It/ Tot. time
10.2 λ	23,814	6	10	14	10	5.9×10^{-3}	0.11 Gb	1.75m	16/27.96m
10.2 λ	23,814	8	6	10	6	6.0×10^{-3}	0.16 Gb	1.13m	16/18.2m
20.4 λ	96,774	10	10	14	10	4.7×10^{-3}	0.50 Gb	7.31m	21/2.56h
20.4 λ	96,774	16	6	10	6	4.5×10^{-3}	0.55 Gb	4.94m	21/1.73h
30 λ	237,606	14	10	14	10	5.5×10^{-3}	1.0 Gb	20.8m	24/8.32h
30 λ	237,606	24	6	10	6	5.4×10^{-3}	1.3 Gb	14.98m	24/5.99h
40.8 λ	390,150	20	10	14	10	4.2×10^{-3}	2.0 Gb	32.71m	27/14.72h
40.8 λ	390,150	32	6	10	6	4.3×10^{-3}	2.4 Gb	23.11m	27/10.4h
50 λ	587,814	24	10	14	10	2.3×10^{-3}	2.9 Gb	56.06m	29/27.1h
50 λ	587,814	40	6	10	6	2.3×10^{-3}	3.8 Gb	40.24m	29/19.45h
100 λ	1,500,000	28	14	18	14	6.2×10^{-3}	7.8 Gb	3.43h	37/127.16h
100 λ Dirichlet	1,500,000	28	14	18	14	4.1×10^{-3}	2.4 Gb	1.58h	17/26.93h

Table 8: Accelerated solvers for the bean-shaped geometry under plane wave incidence of direction $(-\frac{\sqrt{3}}{3}, -\frac{\sqrt{3}}{3}, -\frac{\sqrt{3}}{3})$, using the ICFIE-R formulation implemented with Algorithm III.

Sphere	Our solver	FMM
size (in wavelength λ)	50	50
number of unknowns	618,246	619,520
maximum error	1.0×10^{-4}	1.0×10^{-4}
time required for...		
...construction of the interpolating splines	35 s	
...evaluation of adjacent interactions	945 s	
...evaluation of equivalent source intensities	53 s	
...computations of convolutions	15 s	
...subtraction of adjacent FFTs	86 s	
...evaluation of surface values	9 s	
total acceleration time	163 s	521 s
total time integration	1142 s	
total time per iteration	1240 s	

Table 9: Computing-time requirements of various portions of our algorithm and comparison between the acceleration portions of the present solver for scattering problems with Dirichlet boundary conditions and a recent FMM implementation [19]. Note that FMM is only an acceleration method: it does not provide in itself a full integration or scattering solver.

and gradients of Green's functions evaluated at pairs of sources distributed on surfaces we chose to present a meaningful comparison with the iplementation of our accelerated evaluation of the combined single and double layer potentials that enters the boundary integral formulation of scattering problems with Dirichlet boundary conditions. The computational times required by various stages of our integration algorithm are detailed in the rows in the middle column of Table 9. As it can be seen from this table, the most expensive part of our algorithm is related to the evaluation of the adjacent interactions; the acceleration stage of our algorithm, on the other hand, merely amounts to a small fraction (13% in the present case) of the overall computational time. Table 9 includes a comparison of the acceleration stage of our solver to the computing times and accuracies reported in Table 6 of reference [19]: both of these algorithms are acceleration methods applied to evaluation of interations of a total of approximately 620,000 sources distributed on a sphere 50λ in diameter. (The results [19] were obtained on a 2.66 GHz computer with 2Gb RAM, whose speed is comparable to the one we used). In contrast with the numerical experiments in [19] the computational times we have reported throughout this text (as well as the "total time per iteration" reported in Table 9) correspond to the evaluation of boundary integral operators; our accelerated algorithms, in turn, include an acceleration stage. Except for the row labeled "total acceleration time", all the rows in the column labeled "FMM" are empty: the FMM is just an acceleration strategy—it does not provide a full integration method or scattering solver. Of the total computational time, our acceleration procedure performed via equivalent sources and sparse 3D FFTs takes 163 sec which is significantly *faster* than the wide-band FMM 521 sec computing time reported in reference [19].

In order to further put in perspective the character of our accelerated solvers we finally present in Table 10 comparisons between the performance of our scattering solvers for sound-hard problems to those of solvers based on Galerkin discretizations (Boundary Element Method) and acceleration techniques that rely on High Frequency Fast Multipole Method (HF FMM) and Hierarchical ($\mathcal{H}$) Matrices for sound-hard scattering problem [4]. The results presented in [4] concerned a scattering experiment related to an ellongated cylindrical structure partially immersed in water for which point sources inside the scatterer were considered in order to facilitate the evaluation of the errors on the surface of the scatterer. We note that, for such incident fields, the solutions of the integral equations considered are smooth: they equal the very incident field. Fpr comparison we considered

a similar sound-hard configuration where, for simplicity, the scatterer was taken to be an ellipsoid of size $D \times D/2 \times D/2$ where $D = 36\lambda$—whose acoustical surface area is approximately equal to that of the largest scattering experiments presented in [4]. Indeed, the largest scatering problem reported in [4] consisted of a structure for which discretizations of 10 points/wavelength amounted to 170,000 total unknowns, which translates into an acoustical surface area of $1,700\ \lambda^2$. Using the approximate formula for the surface area of an ellipsoid of semi-axes a, b, c in the form of the Thomsen's formula $A \approx 4\pi \left(\frac{a^p b^p + b^p c^p + c^p a^p}{3}\right)^{\frac{1}{p}}$ where $p \approx 1.6075$ we get that the acoustical surface area of the ellipsoid of size $D \times D/2 \times D/2$ with $D = 36\lambda$ is approximately $1,738\ \lambda^2$.

In order to evaluate the errors of their solvers, the authors in [4] used the point-source (monopole) test which allows for direct evaluations of the errors on the boundary of the scatterers. We present in what follows the details of this test in our context. For the ellipsoid scatterer described above we considered radiating solutions of the Helmholtz equation in the form of monopoles $p(\mathbf{x}) = G_k(\mathbf{x}-\mathbf{x}_0)$ where $\mathbf{x}_0$ is located inside the scatterer (specifically, the ellipsoid has major axes of sizes 1,0.5, and 0.5 and the monopole was centered at $\mathbf{x}_0 = (0.8, 0, 0)$). For such boundary values our DCFIE-R in equation (22) becomes

$$\frac{i\eta}{2} p - i\eta D_k p - (\mathcal{R} \circ N_k) p = -i\eta\, S_k(\partial p/\partial n) + 1/2\, \mathcal{R}(\partial p/\partial n) + (\mathcal{R} \circ D_k')(\partial p/\partial n) \text{ on } \Gamma, \qquad (47)$$

where $\mathcal{R} = S_{ik/2}$ and $\eta = 1$. In order to assess the accuracy of an integral solver, equation (47) is viewed as an integral equation with unknown p and for a given discretization (be it based on Galerkin or Nyström discretizations) a solution p^{comp} is computed via an iterative solver and compared against the exact solution p—which is the monopole itself. For a given discretization, the following norm on the boundary Γ is used in [4] and in Table 10:

$$\varepsilon_2 = \frac{\|p^{comp} - p\|_2}{\|p\|_2}. \qquad (48)$$

The results reported in Table 6 or reference [4], some of which are reproduced in the columns labeled "HF FMM" and "$\mathcal{H}$-matrices" in Table 10, correspond to problems that require 170,000 unknowns (at about 10 points/wavelength) and whose ε_2 errors of about 1.5% using Galerkin discretizations (BEM) and the classical DCFIE formulations —-that is $\mathcal{R} = I$ and $\eta = k$ in equations (47). The authors reported in [4] the set-up time and the time of a matrix-vector product. However, there is no mentioning in [4] of the total computational times required by their solvers. Unfortunately, that contribution does not provide an indication of the manner in which the computing times (set-up, Matrix-Vector product times and associated numbers of iterations) depend on the overall error tolerances imposed. Furthermore, the use of half-space Green's functions in [4] is more advantageous for both the HF FMM and $\mathcal{H}$-matrices algorithms on account of the faster decay of such Green's functions. For our own algorithms, some such statistics are as follows: using the DCFIE equations (the same as the one used in [4]), we need a total of 37,446 unknowns to reach an error $\varepsilon_2 = 1.29\%$ and the cost of a matrix-vector product is 102 sec; the GMRES solver required 31 iterations and a total time of 3,160 sec to reach the accuracy above. On the other hand, using the DCFIE-R formulations, errors of $\varepsilon_2 = 1.6\%$, $\varepsilon_2 = 0.38\%$ and $\varepsilon_2 = 0.041\%$ result from our solver for a total of 37,446 unknowns , 96,774 unknowns and respectively 218,886 unknowns, with total memory requirements of 0.517 Gb, 1.2 Gb and 2 Gb, respectively. The number of iterations and total computational times required by our DCFIE-R solvers for each discretization are 13/2020 sec, 11/3780 sec, and respectively 9/8851 sec.

We note that owing to their high-order nature, our solvers require much fewer unknowns per wavelength to reach the same levels of accuracy; increasing the number of unknowns per wavelength

DCFIE $\varepsilon_2 = 1.2\%$			HF FMM [4] $\varepsilon_2 \approx 1.5\%$			$\mathcal{H}$-matrices [4] $\varepsilon_2 \approx 1.5\%$		
Set-up time	MV-prod time	Mem	Set-up time	MV-prod time	Mem	Set-up time	MV-prod time	Mem
None	102	0.41	3918	136.8	1.62	91136	2.05	6.26

Table 10: Comparison between the CFIE algorithm, HF FMM BEM solvers [4], and $\mathcal{H}$-matrices BEM solvers [4], CPU times (in seconds) and memory usage (in Gb); the latter solvers use discretizations of 10 points/λ corresponding to about 170,000 unknowns to produce solutions with ε_2 accuracy of approximately 1.5%.

our solvers produce more accurate results. We conclude from the results presented in Table 10 that our solvers which are based on accelerated techniques for the DCFIE and DCFIE-R formulations reach the same lavel of accuracy as the BEM solvers accelerated by either HF FMM or $\mathcal{H}$-matrices in shorter computational times: on the one hand, since one matrix-vector product of our solvers is faster than that of the HF FMM, our solvers outperform the BEM solvers accelerated by HF FMM; on the other hand, the BEM solvers accelerated by $\mathcal{H}$-matrices would outperform our solvers for problems that required more than 912 GMRES iterations.

7 Conclusions

This paper introduced novel ICFIE-R and DCFIE-R formulations for the solution of acoustic scattering problems with Neumann boundary conditions. The resulting integral operators possess excellent eigenvalues clustering properties, leading to small numbers of GMRES iterations and, in contrast with the classical CFIE and ICFIE formulations, to iteration numbers that do not grow as discretizations are refined for a fixed frequency. For a given discretization, the errors incurred by our implementation are of the same order as those resulting from the classical Combined Field Integral Equation counterparts. Thus, the important gains in computational cost arising from the new regularized formulation do not impact on accuracy, and therefore make the novel Regularized Combined Field Integral Equations a highly competitive alternative to classical algorithms for solution of sound-hard scattering problems.

Acknowledgments

The authors gratefully acknowledge support from NSF and AFOSR.

References

[1] Amini, S, and P. Harris, A comparison between various boundary integral formulations of the exterior acoustic problem, *Computer Meth. Appl. Mech. Eng. 84*, 1990, 59-75

[2] Antoine X. and Darbas M., "Generalized combined field integral equations for the iterative solution of the three-dimensional Helmholtz equation", in *Mathematical modeling and numerical analysis, 41*, 2007, pp. 147–167.

[3] Antoine, X., Darbas, M., *Alternative integral equations for the iterative solution of acoustic scattering problems*, Q. Jl. Mech. Appl. Math. 58 (2005), no. 1, 107-128

[4] Brunner, D., M. Junge, P. Rapp, M. Bebendorf, and L. Gaul, *Comparison of the fast multipole method with hierarchical matrices for the Helmholtz-BEM*, CMES, vol. 58, no. 2, 131-158, (2010).

[5] Benzi, M., and M. Tuma, "A sparse approximate inverse preconditioner for nonsymmetric linear systems", *SIAM J.Sci. Comput., 3*, vol. 19, 1998, pp 968–994.

[6] E. Bleszynski, M. Bleszynski, and T. Jaroszewicz, AIM: Adaptive integral method for solving large-scale electromagnetic scattering and radiation problems, *Radio Science* **31**, 5, pp. 1225–1251 (1996).

[7] Brackhage, H., and P. Werner, Uber das Dirichletsche Aussenraumproblem fur die Helmholtsche Schwingungsgleichung, *Arch.Math*, 16, 325-329, 1965.

[8] Bruno, O., and L. Kunyansky, Surface scattering in three dimensions: an accelerated high-order solver, *R. Soc. Lon. Proc. Ser. A Math. Phys. Eng. Sci., 2016*, 2921-2934, 2001.

[9] Bruno, O. P. and Kunyansky, L., "A fast, high-order algorithm for the solution of surface scattering problems: basic implementation, tests and applications", *J. Computat. Phys. 169*, (2001) pp. 80–110.

[10] Bruno, O., Elling, T., Paffenroth, R., Turc, C., *Electromagnetic integral equations requiring small numbers of Krylov-subspace iterations*, J. Comput. Phys, 228 (17), 2009, 6169-6183.

[11] O. Bruno, Y. Han and M. Pohlman, *Accurate, high-order representation of complex three-dimensional surfaces via Fourier-Continuation analysis*; Journal of Computational Physics **227** (2007) 1094–1125.

[12] Anand, A., Ovall, J., Turc, C., *Well-conditioned boundary integral equations for two-dimensional sound-hard scattering problems in domains with corners*, to appear in Journal Integral Equations and Applications, 2011.

[13] Burton, A., Miller J., *The application of integral equation methods to the numerical solution of some exterior boundary-value problems*, Proc. Royal Soc. London 323 (1971), 201-210

[14] Burton, A., Numerical solution of acoustic radiation problems, *NPL Contract Rept. OC5/S35 National Physical Laboratory, Teddington, Middlesex*, (1976).

[15] Chen, G., and J. Zhou, "Boundary element methods", Academic Press, Harcourt Press Jovanovitch Publishers, 1992.

[16] Calderón, A., *The multipole expansion of radiation fields*, Arch. Rat. Mech. Anal. 3 (1954), 523-537

[17] Carpentieri, B., *A Matrix-free Two-grid Preconditioner for Solving Boundary Integral Equations in Electromagnetism*, Computing, 77 (2006), 275-296

[18] Carpentieri, B., Duff, I., Giraud, L., Sylvand, G., *Combining fast multipoles techniques and an approximate inverse preconditioner for large electromagnetism calculations*, SIAM J.Sci. Comput., 27 (2005), no. 3, 774-792

[19] Cheng, H., et al., *A wideband fast multipole method for Helmholtz equation in three dimensions*, J. Comput. Phys. 216 (2006), no. 1, 300-325.

[20] Chew, W. C., Jin, J., Michielssen, E., and J. Song, Fast and efficient algorithms in computational electromagnetics, *Artech House, Norwood*, 2001

[21] Christiansen, S., Nédélec, J. C., Des préconditioneurs pour la résolution numérique des équations intégrales de frontière de l'acoustique, *C.R. Acad. Sci. Paris, Sér. I 330*, 2000, 617-622

[22] Colton, D., Kress, R., Integral equation methods in scattering theory, *John Wiley & Sons, Inc., New York*, (1983)

[23] Kress, R., *On the numerical solution of a hypersingular integral equation in scattering theory*, J. Comput. Appl. Math 61 (1995), 345-360

[24] Kress, R., Minimizing the condition number of boundary integral operators in acoustic and electromagnetic scattering ,*Q. Jl. Mech. Appl. Math.*, 38, 323-341, 1985.

[25] Lee, J., Zhang, J., Lu, C., *Sparse inverse preconditioning of multilevel fast multipole algorithm for hybrid integral equations in electromagnetism*, IEEE Trans. Antennas Propag. 52 (2004), 2277-2286

[26] McLean, S., Strongly elliptic systems and boundary integral equations, Cambridge University Press, 2000.

[27] Nédélec, J. C., *Acoustic and electromagnetic equations*, Springer Verlag, New York, 2001.

[28] Panich, I., On the question of the solvability of the exterior boundary problem for the wave equation and Maxwell's equation, *Uspekhi Mat. Nauk 20*, (1965), 221-226

[29] Rokhlin, V., *Diagonal Form of Translation Operators for the Helmholtz equation in Three Dimensions, Applied and Computational Harmonic Analysis* **1**, 82–93, 1993

[30] Saad, Y., and M. H. Schultz, "GMRES: A generalized minimal residual algorithm for solving non-symmetric linear systems", *SIAM J. Sci. Stat. Comput., 3*, vol. 7, 1986, 856–869.

[31] J. M. Song, C. C. Lu, W. C. Chew and S. W. Lee, *Fast Illinois Solver Code,* IEEE Antennas and Propagation Magazine **40**, 27-34, 1998.

[32] Steinbach, O., and W. L. Wendland, "The construction of some efficient preconditioners in the boundary element method", in *Adv. Comput. Math., 9*, no. 1–2, 1998, pp. 191–216.

[33] Volakis, J., Sertel, K., *Incomplete LU preconditioner for FMM implementation*, Microwave Opt. Tech. Lett. 26 (2000), 265-267

[34] Yla-Oijala, P and Jarvenpaa, S., *Iterative solution of high-order boundary element method for acoustic impedance boundary value problems*, Journal Sound and Vibration, 291 (2006), 824–843.